
PARALLEL REPRESENTATION OF CONTEXT AND MULTIPLE CONTEXT-DEPENDENT VALUES IN VENTRO-MEDIAL PREFRONTAL CORTEX

Nir Moneta^{1,3,4*}, Mona M. Garvert^{1,4,5,6}, Hauke R. Heekeren², and Nicolas W. Schuck^{1,4*}

¹Max Planck Research Group NeuroCode, Max Planck Institute for Human Development, 14195 Berlin, Germany

²Department of Education and Psychology, Freie Universität Berlin, 14195 Berlin, Germany

³Einstein Center for Neurosciences Berlin, Charité Universitätsmedizin Berlin, 10117, Berlin, Germany

⁴Max Planck UCL Centre for Computational Psychiatry and Ageing Research, Berlin, 14195 Berlin, Germany

⁵Department of Psychology, Max Planck Institute for Human Cognitive and Brain Sciences, 04103 Leipzig, Germany

⁶Wellcome Centre for Integrative Neuroimaging, FMRIB, University of Oxford, Oxford, United Kingdom

*Corresponding authors, email moneta@mpib-berlin.mpg.de and schuck@mpib-berlin.mpg.de

March 17, 2021

Abstract

1 **Value representations in ventromedial prefrontal-cortex (vmPFC) are known to guide**
2 **decisions. But how preferable available options are depends on one's current task. Goal-**
3 **directed behavior, which involves changing between different task-contexts, therefore**
4 **requires to know how valuable the same options will be in different contexts. We**
5 **tested whether multiple task-dependent values influence behavior and asked if they are**
6 **integrated into a single value representation or are co-represented in parallel within**
7 **vmPFC signals. Thirty five participants alternated between tasks in which stimulus**
8 **color or motion predicted rewards. Our results provide behavioral and neural evidence**
9 **for co-activation of both contextually-relevant and -irrelevant values, and suggest a link**
10 **between multivariate neural representations and the influence of the irrelevant context**
11 **and its associated value on behavior. Importantly, current task context could be decoded**
12 **from the same region, and better context-decodability was associated with stronger**
13 **(relevant-)value representations. Evidence for choice conflicts was found only in the**
14 **motor cortex, where the competing values are likely resolved into action.**

15 Introduction

16 Decisions are always made within the context of a given task. Even a simple choice between two apples will
17 depend on whether the task is to find a snack, for which their color might indicate the desired sweetness, or to buy
18 ingredients for a cake, for which a crisp texture might be more crucial. In other words, the same objects can yield
19 different outcomes under different task contexts. Context-dependent decision-making therefore requires to retrieve
20 not only the outcomes that are associated with different objects. Rather, it is necessary to maintain separate
21 outcome expectations for the same choice option, and to know in which task context which outcome expectation
22 is relevant.

23 Computing the reward a choice will yield given a task context is at the core of decisions [e.g. 1]. In line with
24 this idea, previous studies have shown in a variety of species that the ventromedial prefrontal cortex (vmPFC)
25 represents this so-called expected value (EV) [2–7], and thereby plays a crucial role in determining choices [8]. It
26 is also known that the brain's attentional control network enhances the processing of features that are relevant
27 given the current task context [9, 10], and that this helps to shape which features influence EV representations in
28 vmPFC [11–13]. Moreover, the vmPFC seems to also represent the EV of different features in a common currency
29 [14, 15]; and thus is necessary for integrating the expectations from different reward predicting features of the
30 same object [16–18]. It remains unclear however, how context-irrelevant value expectations of presented features,
31 i.e. rewards that would be obtained in a different task-context, might affect neural representations in vmPFC.

32 This is particularly relevant because we often have to do more than one task within the same environment, such as
33 shopping in the same supermarket for different purposes. Thus we have to switch between the values that are
34 relevant in the different contexts. Moreover, the separation between tasks can often be less than perfect, which can
35 then lead to processing of task-irrelevant aspects. In line with this idea, several studies have shown that decisions
36 are influenced by contextually-irrelevant information, and traces of the distracting features in cortical regions
37 responsible on task execution [19–23]. Similarly, task-irrelevant valuation has been shown to influence attentional
38 selection [24] as well as activity in posterior parietal [25] or ventromedial prefrontal cortex [26]. This raises the
39 possibility that vmPFC represents different value expectations that could occur in different task contexts at the
40 same time. In the present study we therefore investigated whether the vmPFC maintains multiple task-dependent
41 values during choice, and how these representations influence choices, interact with the encoding of the relevant
42 task-context, and with each other.

43 Previous research has indeed suggested that the role of vmPFC in decision making seems not to be restricted to
44 representing economic values. Rather, other aspects of the current task might be encoded in this region as well
45 [27–31]. Of particular relevance, a number of investigations have indicated that vmPFC and adjacent overlapping
46 medial orbitofrontal cortex represents the current context or task state in humans [32–35]. This task state effectively
47 encodes which features are currently relevant and thereby determines which value expectations will guide behavior.
48 Note, however, that these value and task-state accounts do not need to be mutually exclusive, but rather might
49 reflect multiplexed representations within the neural activity of the vmPFC/OFC [36, 37]. Conceptualizing the
50 role of vmPFC as representing possible task states therefore bridges beyond its traditional role as controller of
51 economic value to a more complex role of parallel representation of task-related information, EV included.

52 If neural activity in vmPFC goes beyond signalling a single EV by representing more complex task structure,
53 then it suggests that the task-context is represented in addition to the values. We therefore hypothesized that
54 vmPFC indeed simultaneously represents the task-context, as well as task-relevant and task-irrelevant values.
55 This idea – that values and task-context co-occur and interact – also predicts that a stronger activation of the
56 relevant task-context will enhance the representation of task-relevant values. We investigated this question using
57 a multi-feature choice task in which different features of the same stimulus predicted different outcomes and a
58 task-context cue modulated which feature was relevant. We hypothesized that values associated with contextually
59 irrelevant features affect value representations in vmPFC. Moreover, we tested whether different possible EVs were

60 integrated into a single value representation or processed in parallel. The former would support a unique role of
 61 the vmPFC for representing *only* the EV of choice, whereas the latter would indicate that the vmPFC encodes
 62 several aspects of a complex task structure, including separate value representations for the currently relevant and
 63 irrelevant task contexts.

64 Results

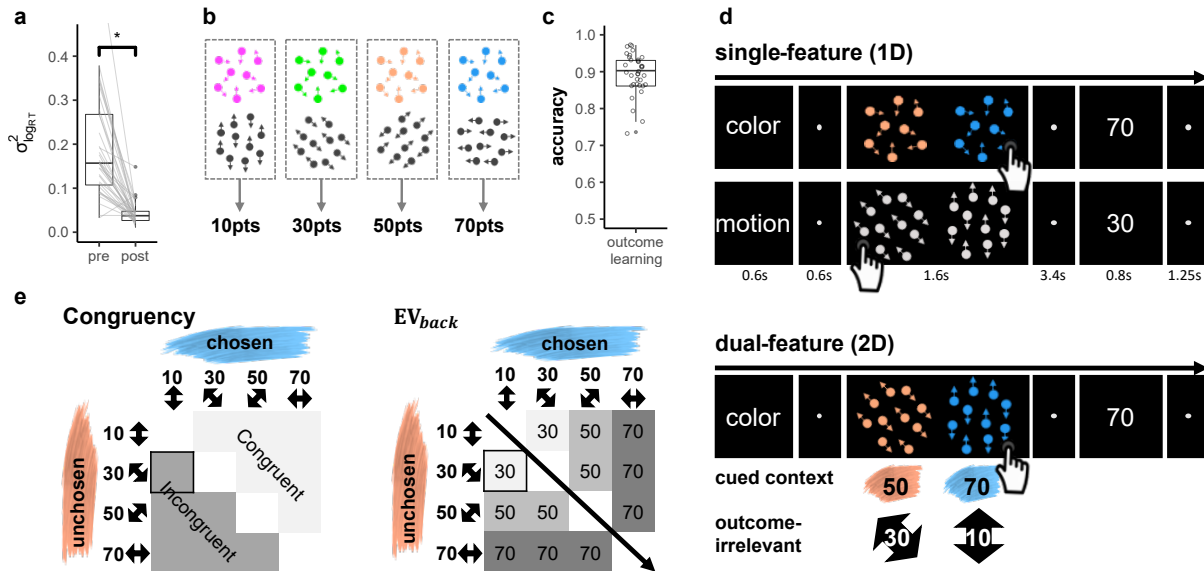


Figure 1: Task and Design **a.** Staircasing procedure reduced differences in detection speed between features. Depicted is the variance of reaction times (RTs) across different color and motion features (y axis). While participants' RTs were markedly different for different features before staircasing (pre), a significant reduction in RT differences was observed after the procedure (post). The staircasing procedure was performed before value learning. RT-variance was computed by summing the squared difference of each feature's RT and the general mean RT per participant. $N = 35$, $p < .001$. **b.** The task included eight features, four color and four motion directions. After the stair-casing procedure, a specific reward was assigned to each motion and each color, such that one feature from each of the contexts had the same value as it was associated with the same reward. Feature values were counterbalanced across participants. **c.** Participants were trained on feature values shown in (b) and achieved near ceiling accuracy in choosing the highest valued feature afterwards ($\mu = .89$, $\sigma = .06$). **d.** Single- and dual-feature trials (1D, 2D, respectively). Each trial started with a cue of the relevant context (Color or Motion, 0.6s), followed by a short fixation circle (0.6s). Participants were then presented with a choice between two clouds (1.6s). Each cloud had only one feature in 1D trials (colored dots, but random motion, or directed motion, but gray dots, top) and two features for 2D trials (motion and color, bottom). Participants were instructed to make a decision between the two clouds based on the cued context and ignore the other. Choices were followed by a fixation period (3.4s) and the value associated with the chosen cloud's feature of the cued context (0.8s). After another short fixation (1.25s) the next trial started. **e.** Variations in values irrelevant in the present task context of a 2D trial. For each feature pair (e.g. blue and orange), all possible context-irrelevant feature-combinations were included in the task, except the same feature on both sides. Congruency (left): trials were separated into those in which the irrelevant features favored the same choice as the relevant features (congruent trials), or not (incongruent trials). EV_{back} (right): based on this factor, the trials were characterized by different hypothetically expected values of the contextually-irrelevant features, i.e. the maximum value of both irrelevant features. Crucially, EV, EV_{back} and Congruency were orthogonal by design. The example trial presented in (d, bottom) is highlighted.

65 Behavioral results

66 Participants had to judge either the color or motion direction of moving dots on a screen (random dot motion
 67 kinematograms, [e.g. 38]). Four different colors and motion directions were used. Before entering the MRI
 68 scanner, participants performed a stair-casing task in which participants had to indicate which of two shown stimuli
 69 corresponded to a previously cued feature. Motion-coherence and the speed which dots changed from grey to a
 70 target color were adjusted such that the different stimulus features could be discriminated equally fast, both within

71 and between contexts. As intended, this led to significantly reduced differences in reaction times (RTs) between
72 the eight stimulus features ($t_{(34)} = 7.29$, $p < .001$, Fig.1a), also when tested for each button separately ($t_{(34)} =$
73 Left: 6.52, Right: 7.70, $ps < .001$, Fig. S1d)

74 Only then, participants learned to associate each color and motion feature with a fixed number of points (10,
75 30, 50 or 70 points), whereby one motion direction and one color each led to the same reward (counterbalanced
76 across participants, Fig.1b). To this end, participants had to make a choice between clouds that had only one
77 feature-type, while the other feature type was absent or ambiguous (clouds were grey in motion clouds and moved
78 randomly in color clouds). To encourage mapping of all features on a unitary value scale, choices in this part (and
79 only here) also had to be made between contexts (e.g. between a green and a horizontal-moving cloud). At the
80 end of the learning phase, participants achieved near-ceiling accuracy in choosing the cloud with the highest valued
81 feature ($\mu = .89$, $\sigma = 0.06$, t-test against chance: $t_{(34)} = 41.8$, $p < .001$, Fig. 1c), also when tested separately for
82 Color, Motion and across context ($\mu = .88, .87, .83$, $\sigma = .09, .1, .1$, t-test against chance: $t_{(34)} = 23.9, 20.4, 19.9$,
83 $ps < .001$, respectively, Fig. S1e). Once inside the MRI scanner, one additional training block ensured changes in
84 presentation mode did not induce feature-specific RT changes ($F_{(7,202)} = 1.06$, $p = 0.392$). These procedures
85 made sure that participants began the main experiment inside the MRI scanner with firm knowledge of feature
86 values; and that RT differences would not reflect perceptual differences, but could be attributed to the associated
87 values. Additional information about the pre-scanning phase can be found in Online Methods and in Fig.S1.

88 During the main task, participants had to select one of two dot motion clouds. In each trial participants were first
89 cued whether a decision should be made based on color or motion features, and then had to choose the cloud that
90 would lead to the largest number of points. Following their choice, participants received the points corresponding
91 to the value associated with the chosen cloud's relevant feature. To reduce complexity, the two features of the
92 *cued task-context* always had a value difference of 20, i.e. the choices on the cued context were only between
93 values of 10 vs. 30, 30 vs. 50 or 50 vs. 70. One third of the trials consisted of a choice between single-feature
94 clouds of the same context (henceforth: 1D trials, Fig.1d, top). All other trials were dual-feature trials, i.e. each
95 cloud had a color *and* a motion direction at the same time (henceforth: 2D trials, Fig.1d bottom), but only the
96 color or motion features mattered as indicated by the cue. Thus, while 2D trials involved four features in total
97 (two clouds with two features each), only the two color *or* two motion features were relevant for determining the
98 outcome. The cued context stayed the same for a minimum of four and a maximum of seven trials. Importantly,
99 for each comparison of relevant features, we varied which values were associated with the features of the *irrelevant*
100 context, such that each relevant value was paired with all possible irrelevant values (Fig.1e). Consider, for instance,
101 a color trial in which the color shown on the left side led to 50 points and the color on the right side led to 70
102 points. While motion directions in this trial did not have any impact on the outcome, they might nevertheless
103 influence behavior. Specifically, they could favor the same side as the colors or not (Congruent vs Incongruent
104 trials, see Fig.1e left), and have larger or smaller values compared to the color features (Fig.1e right).

105 We investigated the impact of these factors on RTs in correct 2D trials, where the extensive training ensured
106 near-ceiling performance throughout the main task ($\mu = 0.91$, $\sigma = 0.05$, t-test against chance: $t_{(34)} = 48.48$,
107 $p < .0001$, Fig.2a). RTs were log transformed to approximate normality and analysed using mixed effects models
108 with nuisance regressors for choice side (left/right), time on task (trial number), differences between attentional
109 contexts (color/motion) and number of trials since the last context switch. We used a hierarchical model comparison
110 approach to assess the effects of (1) the objective value of the chosen option (or: EV), i.e. points associated with
111 the features on the cued context; (2) the maximum points that could have been obtained if the irrelevant features
112 were the relevant ones (the expected value of the background, henceforth: EV_{back} , Fig 1e left), and (3) whether
113 the irrelevant features favored the same side as the relevant ones or not (Congruency, Fig. 1e right). Any effect
114 of the latter two factors would indicate that outcome associations that were irrelevant in the current context
115 nevertheless influence behavior, and therefore could be represented in vmPFC.

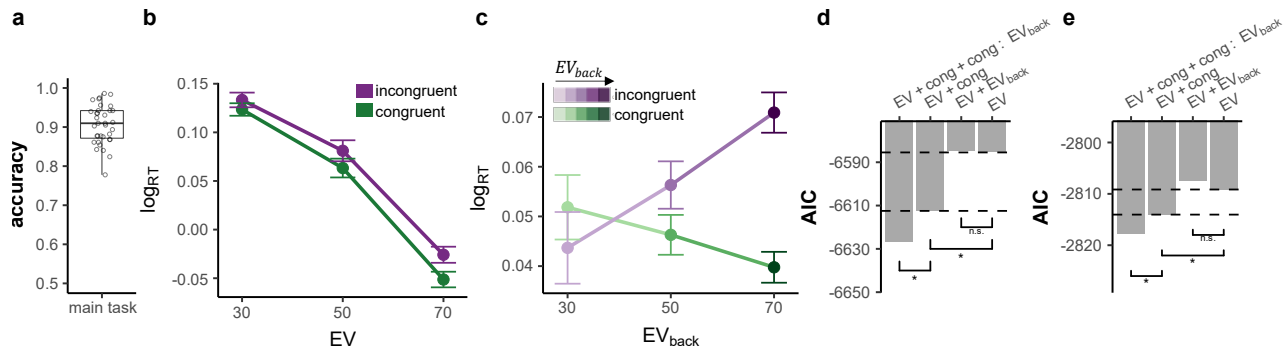


Figure 2: Behavioral results a. Participants were at near-ceiling performance throughout the main task, $\mu = 0.905, \sigma = 0.05$. b. Participants reacted faster the higher the EV (x-axis) and slower to incongruent (purple) compared to congruent (green) trials. An interaction of EV \times Congruency indicated stronger Congruency effect for higher EV ($p = .037$). Error bars represent corrected within subject SEMs [39, 40]. c. The Congruency effect was modulated by EV_{back} , i.e. the more participants could expect to receive from the ignored context, the slower they were when the contexts disagreed and respectively faster when contexts agreed (x axis, shades of colours). Error bars represent corrected within subject SEMs [39, 40]. d. Hierarchical model comparison for the main sample showed that including Congruency ($p < .001$), yet not EV_{back} ($p = .27$), improved model fit. Including then an additional interaction of Congruency \times EV_{back} improved the fit even more ($p < .001$). e. We replicated the behavioral results in an independent sample of 21 participants outside of the MRI scanner. Including Congruency ($p = .009$), yet not EV_{back} ($p = .63$), improved model fit. Including an additional interaction of Congruency \times EV_{back} explained the data best ($p = .017$).

116 A baseline model including only the factor EV indicated that participants reacted faster in trials that yielded bigger
 117 rewards ($\chi^2_{(1)} = 1374.6, p < .001$, Fig. 2b), in line with previous literature [41–43]. In the first step, we added
 118 either Congruency or EV_{back} to the model. We found that Congruency also affected RTs, i.e. participants reacted
 119 slower to incongruent compared to congruent trials (t-test: $t_{(39)} = 4.59, p < .001$, likelihood ratio test to assess
 120 improved model fit: $\chi^2_{(1)} = 29.9, p < .001$, Fig. 2b). Interestingly, neither adding a main effect for EV_{back} nor the
 121 interaction of EV \times EV_{back} improved model fit (LR-test with added terms: $\chi^2_{(1)} = 1.21, p = .27$ and $\chi^2_{(1)} = .01$,
 122 $p = 0.9$ respectively), meaning neither larger irrelevant values, nor their similarity to the objective value influenced
 123 participants' behavior.

124 In a second step, we investigated if the Congruency effect represents merely an agreement between the contexts,
 125 or if it interacted with the expected value of the best choice in the other context, i.e. the points associated with
 126 the most valuable irrelevant stimulus feature (EV_{back}). Indeed, we found that the higher EV_{back} was, the faster
 127 participants were on congruent trials. In incongruent trials, however, higher EV_{back} had the opposite effect (Fig. 2c,
 128 LR-test of model with added interaction: $\chi^2_{(1)} = 18.19, p < .001$). We found no effect of the value associated with
 129 the other, lower valued irrelevant feature that would not have been chosen (LR-test to baseline model: $\chi^2_{(1)} = 0.92$,
 130 $p = .336$), nor did it interact with Congruency ($\chi^2_{(1)} = 2.76, p = .251$). This means that the expected value of a
 131 'counterfactual' choice resulting from consideration of the irrelevant features mattered, i.e. that the outcome such
 132 a choice could have led to, also influenced reaction times. The hierarchical model comparison is summarized in Fig.
 133 2d. All the effects above also hold when running the models nested across the levels of EV (as well as Block and
 134 Context, see Fig. S2). All nuisance regressors had a significant effect on RT (all $p < 0.03$ in the baseline model).

135 The main behavioral results were replicated in an additional sample of 21 participants that were tested outside
 136 of the MRI scanner (LR-tests: Congruency, $\chi^2_{(1)} = 6.89, p = .009$, $EV_{back}, \chi^2_{(1)} = .23, p = .63$, Congruency \times
 137 $EV_{back}, \chi^2_{(1)} = 5.69, p = .017$, Fig. 2e).

138 We note that similar to the $EV_{back} \times$ Congruency interaction, we also found that higher EV slightly increased
 139 the Congruency effect (Fig. 2b, LR-test: $\chi^2_{(1)} = 4.34, p = .037$). However, the interaction of Congruency \times EV
 140 did not survive model comparison in the replication sample ($\chi^2_{(1)} = 0.23, p = .63$). Alternative regression models
 141 considering for instance within-cloud or between-context value differences did not provide a better fit the RTs

142 (Fig.S3). An exploratory analysis investigating all possible 2-way interactions with all nuisance regressors can be
 143 found in Fig. S4.

144 We took a similar hierarchical approach to model accuracy of participants in 2D trials, using mixed effects models
 145 with the same nuisance regressors as in the RT analysis. This revealed a main effect of EV (baseline model:
 146 $\chi^2_{(1)} = 14.71, p < .001$), indicating higher accuracy for higher EV. Introducing Congruency and then an interaction
 147 of Congruency \times EV_{back} further improved model fit (LR-test: $\chi^2_{(1)} = 66.12, p < .001, \chi^2_{(1)} = 6.99, p = .03$,
 148 respectively), reflecting decreased performance on Incongruent trials, with higher error rates occurring on trials
 149 with higher EV_{back}. Unlike RT, error rates were not modulated by the interaction of EV and Congruency (LR-test
 150 with EV \times Congruency: $\chi^2_{(1)} = 0.05, p = .825$). Out of all nuisance regressors, only switch had an influence on
 151 accuracy ($\chi^2_{(1)} = 10.22, p = .001$, in the baseline model) indicating increasing accuracy with increasing trials since
 152 the last switch trial.

153 In summary, these results indicated that participants did not merely perform a value-based choice among features
 154 on the currently relevant context. Rather, both reaction times and accuracy indicated that participants also
 155 retrieved the values of irrelevant features and computed the resulting counterfactual choice.

156 fMRI results

157 Decoding multivariate value signal

158 **from vmPFC** Our MRI analyses focused on understanding the impact of ir-
 159 relevant reward expectations on value signals in vmPFC. We therefore first sought
 160 to identify a value-sensitive region of interest (ROI) that reflected expected val-
 161 ues in 1D and 2D trials, following common procedures in the literature [e.g. 4].
 162 Specifically, we analyzed the fMRI data using general linear models (GLMs) with
 163 separate onsets and EV parametric modulators for 1D and 2D trials (at stimulus
 164 presentation, see online methods for full model). The union of the EV modulators
 165 for 1D and 2D trials defined a functional ROI for value representations that
 166 encompassed 998 voxels, centered on the vmPFC (Fig. 3a, $p < .0005$, smoothing:
 167 4mm, to match the multivariate analysis), which was transformed to individual sub-
 168 ject space for further analyses (mean number of voxels: 768.14, see online meth-
 169 ods).
 170
 171
 172
 173
 174
 175
 176
 177
 178
 179
 180

181 In the next step we focused on the mul-
 182 tivariate activation patterns in the above-
 183 defined functional ROI. We trained a mul-
 184 tivariate multinomial logistic regression
 185 classifier to distinguish the EVs of accu-
 186 rate 1D trials based on fMRI data acquired approximately 5 seconds after stimulus onset (Fig. 3b; leave-one-run-out

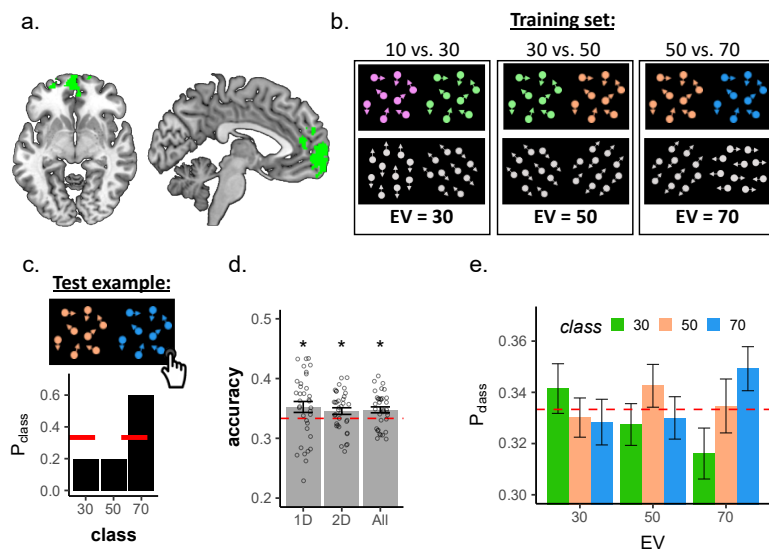


Figure 3: Multivariate value analyses. **a.** The union of the EV parametric modulator allowed us to isolate a cluster in the vmPFC. Displayed coordinates in the figure: $x=-6, z=-6$. **b.** We trained the classifier on behaviorally accurate 1D trials on patterns within the functionally-defined vmPFC ROI. **c.** The classifier yielded for each testing example one probability for each class. **d.** The classifier assigned the highest probability to the correct class (objective EV) significantly above chance for 1D trials, but also generalized to 2D and across all trials ($p = .049, p = .039, p = .007$ respectively). Error bars represent corrected within subject SEMs [39, 40]. **e.** Analyses of all probabilities revealed gradual value similarities. The y-axis represents the probability assigned to each class, colors indicate the classifier class and the x-axis represents the trial type (the objective EV of the trial). As can be seen, the highest probability was assigned to the class corresponding to the objective EV of the trial. Error bars represent corrected within subject SEMs [39, 40]

187 training; see online methods for details). For each testing example, the classifier assigned the probability of each
 188 class given the data (i.e. '30', '50' and '70', which sum up to 1, Fig. 3c). Because the ROI was constructed
 189 such as to contain significant information about EVs, the classifier should predict the correct EV. As expected,
 190 the class with the maximum probability corresponded to the objective outcome more often than chance in 1D
 191 trials ($\mu_{1D} = .35, \sigma_{1D} = .054$). Importantly, EV decoding also generalized to a test set composed of 1D and
 192 2D trials ($\mu_{all} = .35, \sigma_{all} = .029, t_{(34)} = 2.89, p = .007$), and was significant when testing only on 2D trials
 193 ($\mu_{2D} = .35, \sigma_{2D} = .033, t_{(34)} = 2.20, p = .034$, Fig. 3d), even though the training data was restricted to 1D trials.
 194 The following analyses model directly the class probabilities estimated by the classifier. Probabilities were modelled
 195 with beta regression mixed effects models [44]. For technical reasons, we averaged across nuisance regressors used
 196 in behavioral analyses. An exploratory analysis of raw data including nuisance variables showed that they had no
 197 influence and confirmed all model comparison results reported below (see Fig S6 and S8).

198 **Multivariate neural value codes reflect**
 199 **value similarities and are negatively affected**
 200 **by contextually-irrelevant value information.**

201 We next asked whether EVs affected not only the probability of the corresponding class, but also influ-
 202 enced the full probability distribution predicted by the classifier. We reasoned that if the classifier
 203 is decoding the neural code of values, then similarity between the values assigned to the classes
 204 will yield similarity in probabilities associated to those classes. Specifically, we expected not only
 205 that the probability associated with the correct class be highest (e.g. '70'), but also that the probability
 206 associated with the closest class (e.g. '50') would be higher than the probability with the least similar
 207 class (e.g. '30', Fig. 3e). To test our hypothesis, we modelled the probabilities in each trial as a function
 208 of the absolute difference between the objective EV of the trial and the class ($|EV - class|$, i.e. in the above
 209 example with a correct class of 70, the probability for the class 50 will be modelled as condition $70-50=20$
 210 and the probability of 30 as $70-30=40$). This analysis indeed revealed such a value similarity
 211 effect ($\chi^2_{(1)} = 12.74, p < .001$) also when tested separately on 1D and 2D trials ($\chi^2_{(1)} = 14.22,$
 212 $p < .001, \chi^2_{(1)} = 9.99, p = .002$, respectively, Fig. 4a). We compared this value similarity
 213 model to a perceptual model that merely encodes the amount of perceptual overlap between each
 214 training class and 2D testing (irrespective of their corresponding values) and found that our model
 215 explained the data best (Fig. 4b and Fig. S6).

231 Our main hypothesis was that context-irrelevant values might influence neural codes of value in
 232

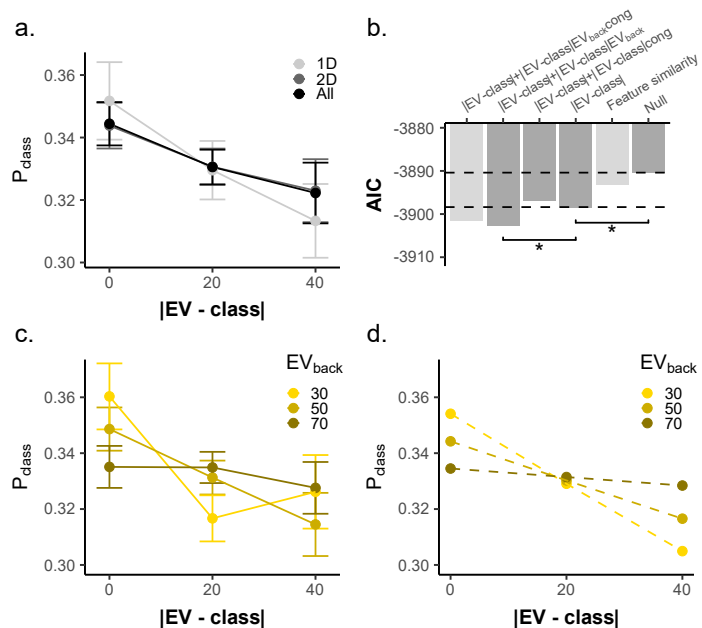


Figure 4: Impact of irrelevant feature values on value representations in vmPFC. a. Larger difference between the decoded class and the objective EV of the trial (x axis) was related to a lower probability assigned to that class (y axis) when tested in 1D, 2D or all trials (all $p < .002$, grey shades). Hence, the multivariate classifier reflected gradual value similarities. Note that when $|EV - class|=0$, P_{class} is the probability assigned to the objective EV of the trial. Error bars represent corrected within subject SEMs [39, 40] b. AIC values of competing models of value probabilities classified from vmPFC. Hierarchical model comparison of 2D trials revealed not only the differences between decoded class and objective EV ($|EV - class|$) improved model fit ($p < .002$), but rather that EV_{back} modulated this effect ($p = .013$). Crucially, Congruency did not directly modulate the value similarity ($p = .446$). Light gray bars represent models outside the hierarchical comparison. Including a 3-way interaction (with both EV_{back} and Congruency) did not provide better AIC score. A perceptual model encoding the feature similarity between each testing trial and the training classes (irrespective of values) did not provide a better AIC score than the value similarity model ($|EV - class|$). c-d. The higher the EV_{back} was, the weaker the effect of value similarity on the classifier's probabilities ($p = .013$). Data presented in (c) and model in (d). Error bars represent corrected within subject SEMs [39, 40].

233 the vmPFC. The experimentally manipulated background values in our task should therefore interact with the EV
234 probabilities decoded from vmPFC. We thus tested the EV classifier only on 2D trials and asked whether the above
235 described value similarity effect was influenced by EV_{back} and/or Congruency. Analogous to our RT analyses, we
236 used a hierarchical model comparison approach and tested if the interaction of value similarity with these factors
237 improved model fit, using χ^2 based LR-tests (Fig. 4b). We found that EV_{back} , but not Congruency, modulated the
238 value similarity effect ($\chi^2_{(1)} = 6.16, p = .013, \chi^2_{(1)} = .58, p = .446$, respectively, Fig. 4c). This effect indicated
239 that the higher the EV_{back} was, the less steep was the value similarity effect. Although including a 3-way interaction
240 also improved model fit over a baseline model (Congruency \times EV_{back} \times |EV-class|, $\chi^2_{(1)} = 7.2, p = .027$), the AIC
241 score did not surpass the model with only the 2-way interaction (-3902.5, -3901.6, respectively). These results also
242 hold when running the models nested within the levels of EV (Fig.S6). Replacing the EV_{back} with a parameter
243 that encodes the presence of the perceptual feature corresponding to EV_{back} in the training class (Similarity_{back}: 1
244 if the feature was preset, 0 otherwise, see Fig. S7) did not provide a better AIC score (-3897.1) than including the
245 value of EV_{back} (-3902.5). Note that main effects of EV_{back} or Congruency would not be sensible to test in this
246 analysis because both factors don't discriminate between the classes, but rather assign the same value to all three
247 probabilities from that trial (which sum to 1).

248 In summary, this indicates that the neural code of value in the vmPFC is affected by contextually-irrelevant value
249 expectations, such that larger alternative values disturb neural value codes in vmPFC more than smaller ones. This
250 was the case even though the alternative value expectations were not relevant in the context of the considered
251 trials. The effect occurred irrespective of the agreement or action-conflict between the relevant and irrelevant
252 values, unlike participants' behaviour, which were mainly driven by Congruency and its interaction with EV_{back} .
253 Our finding suggests that the (counterfactual) value of irrelevant features must have been computed and poses
254 the power to influence neural codes of objective EV in vmPFC.

255 **Larger irrelevant value expectations are related to reduced relevant EV signals, influencing behavior.**

256 While modelling the full probability distribution over values offers important insights, it only indirectly sheds light
257 on the neural representation of the objective EV that reflects participants' choices in correct trials. We next
258 focused on modelling the probability associated with the class corresponding to the objective EV of each 2D trial
259 (henceforth: P_{EV}). This also resolved the statistical issues arising from the dependency of the three classes (i.e.
260 for each trial they sum to 1). As can be inferred by Fig 3e above, the median probability of the objective EV on
261 2D trials was higher than the the average of the other non-EV probabilities ($t_{(34)} = 2.50, p = .017$) In line with
262 the findings reported above, we found that EV_{back} had a negative effect on P_{EV} ($\chi^2_{(1)} = 5.96, p = .015$, Fig. 5a),
263 meaning that higher EV_{back} was associated with a lower probability of the objective EV, P_{EV} . Interestingly, and
264 unlike in the behavioral models, we found that neither Congruency nor its interaction with EV or with EV_{back}
265 influenced P_{EV} ($\chi^2_{(1)} = 0.035, p = .852, \chi^2_{(1)} = 0.48, p = .787, \chi^2_{(1)} = .99, p = .317$, respectively, Fig. 5b).
266 The effect of EV_{back} also holds when running the model nested inside the levels of EV ($\chi^2_{(1)} = 5.99, p = 0.014$,
267 Fig.S8b). A model including an additional regressor that encoded trials in which $EV=EV_{\text{back}}$ (or: match) did not
268 improve model fit, and no evidence for an interaction of the match regressor with the EV_{back} was found (LR test
269 with added terms: $\chi^2_{(1)} = 0.45, p = .502, \chi^2_{(1)} = 0.77, p = .379$, respectively). This might indicate that when
270 value expectations of both contexts matched, there was neither an increase nor a decrease of P_{EV} . Lastly, we
271 verified that replacing EV_{back} with the perception-based Similarity_{back} regressor did not provide a better model fit
272 (AICs: -1229.2, -1223.3, respectively). These findings confirm that EV_{back} is not only disturbing the neural code of
273 values in the vmPFC but also specifically decreases the decodability of the objective EV.

274 As in our behavioral analysis, we evaluated alternative models of P_{EV} that included a factor reflecting within-option
275 or between-context value differences, or alternatives for EV_{back} (Fig.S8). This exploratory analysis revealed that
276 our model provides the best fit for P_{EV} in all cases except when EV_{back} was replaced with the sum of irrelevant
277 values (-1229.6, -1229.2, respectively, Fig. S8). In contrast, AIC scores of behavioral models' favored EV_{back} as
278 modulator of Congruency, over the sum of irrelevant values (-6626.6, -6619.9, respectively, Fig.S3). However, both

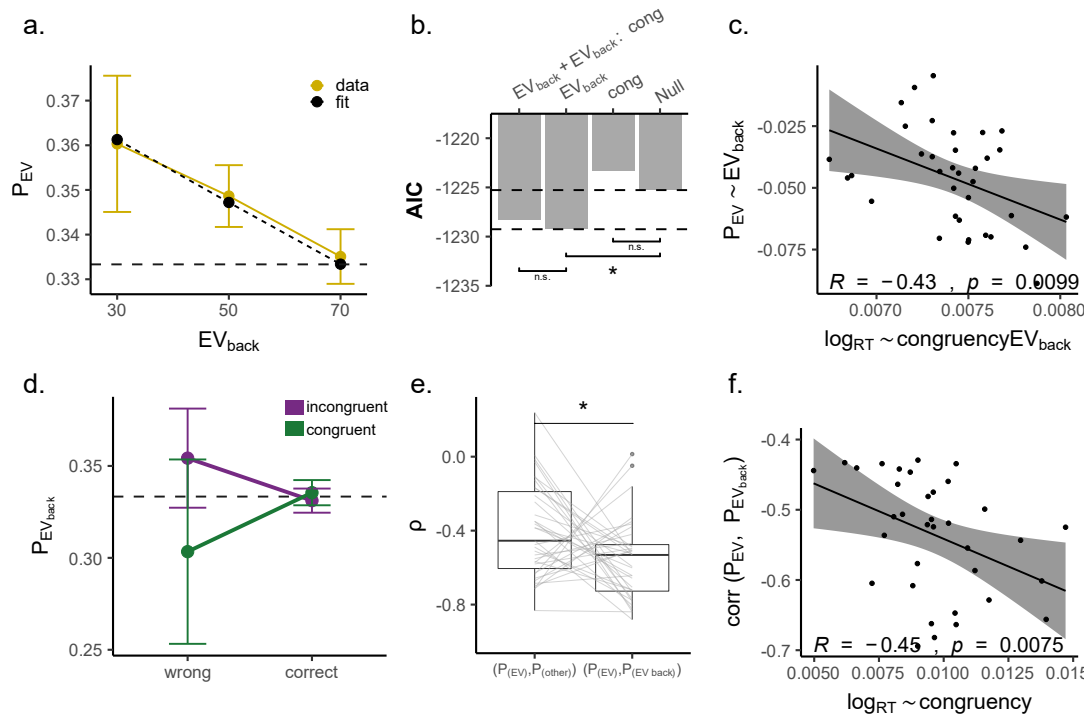


Figure 5: Multivariate results: decoding the EV **a.** Higher EV_{back} was related to a decreased decodability of EV ($p = .015$). Yellow line reflects data, dashed line model fit from mixed effects models described in text. Error bars represent corrected within subject SEMs [39, 40]. **b.** Hierarchical model comparisons revealed that the effect of EV_{back} alone explained data best ($p = .015$) and no main effect or interaction with Congruency was indicated (Congruency main effect, $p = .852$, Congruency $\times EV_{back}$, $p = .317$). **c.** Participants who had a stronger effect of EV_{back} on the EV decodability (y-axis, more negative values indicate stronger decrease of P_{EV} as a result of EV_{back} , see panel a) also had a stronger modulation of EV_{back} on the effect of Congruency on their RT (x-axis, more positive values indicate stronger influence on the slow incongruent and fast congruent trials). **d.** The probability associated with EV_{back} ($P_{EV_{back}}$, y-axis) was increased when participants chose the option based on EV_{back} . Specifically, in incongruent trials (purple), high $P_{EV_{back}}$ was associated a wrong choice, whereas in Congruent trials (green) it was associated with correct choices. This effect is preserved when modeling only wrong trials (main effect of Congruency: $\chi^2_{(1)} = 4.36$, $p = .037$). Error bars represent corrected within subject SEMs [39, 40]. **e.** The correlation of P_{EV} and $P_{EV_{back}}$ was stronger than with P_{Other} , $p = .017$. **f.** Participant that had a stronger (negative) correlation of P_{EV} and $P_{EV_{back}}$ (x-axis, more negative values indicate stronger negative relationship) also had a stronger effect of Congruency on their RT (y-axis, larger values indicate a stronger RT decrease in incongruent compared to congruent trials)

279 parameters were strongly correlated ($\rho = .87$, $\sigma = .004$) and therefore our task was not designed to distinguish
280 between these two alternatives.

281 If the effect of EV_{back} indeed reflects an influence of contextually-irrelevant values on neural representations of the
282 relevant expected value, then this might impact participants' behavior. We therefore asked whether the influence
283 on the representation in vmPFC might relate to participants' reaction times. In line with this idea, we found that
284 participants with a stronger EV_{back} effect on P_{EV} also had a stronger $EV_{back} \times$ Congruency interaction effect on
285 their RT ($r = -.43$, $p = .01$, Fig. 5c).

286 Next, we tested whether vmPFC represents EV_{back} directly. A classifier trained on accurate 2D trials with the
287 labels of EV_{back} could not successfully detect the correct class (t-test against chance: $t_{(34)} = 0.73$, $p = .47$).
288 Note, however, that 2D trials were not fully balanced across the values of EV_{back} (Fig. 1e), which complicated
289 obtaining enough trials for classifier training. We thus turned to look at the probability the classifier trained on 1D
290 trials assigned to the class corresponding to EV_{back} (henceforth: $P_{EV_{back}}$). When focusing only on behaviorally
291 accurate trials, we found no effect of EV nor Congruency on $P_{EV_{back}}$ ($\chi^2_{(1)} = 0.07$, $p = .794$, $\chi^2_{(1)} = 0.00$, $p = .987$
292 respectively). However, motivated by our behavioral analyses that indicated an influence of the irrelevant context

293 on accuracy, we asked whether $P_{EV_{back}}$ was different on behaviorally wrong or incongruent trials. We found an
 294 interaction of accuracy \times Congruency ($\chi^2_{(1)} = 4.51, p = .034$, Fig. 5d) that indicated increased $P_{EV_{back}}$ for
 295 accurate congruent trials and a decrease for wrong incongruent trials. Effectively, this means that in trials in which
 296 participants erroneously chose the option with higher valued irrelevant features, $P_{EV_{back}}$ was increased.

297 **Parallel representation of task-relevant and task-irrelevant expected values in vmPFC.** Our previous
 298 analyses indicated that the probability of the objective EV decreased with increasing EV_{back} . This decrease
 299 could reflect a general disturbance of the value retrieval process caused by the distraction of competing values.
 300 Alternatively, if the irrelevant values are represented within the same neural code as the objective EV, then the
 301 probability assigned to the class corresponding to EV_{back} would increase in exchange for a decrease in P_{EV} – even
 302 though the classifier was trained in the absence of task-irrelevant values, i.e. the objective EV of 1D trials. In
 303 order to test this idea, we took the same trained classifier and tested it only on trials in which $EV \neq EV_{back}$, i.e.
 304 in which the value expected in the current task context was different than the value that would be expected for
 305 the same choice in a different task-context. This allowed us to re-label the classes of each trial to P_{EV} , $P_{EV_{back}}$
 306 and P_{other} , where 'other' corresponds to the class that is neither the EV nor EV_{back} of the trial, and examine
 307 directly the correlation between each pair of classes. To prevent a bias between the classes, we only included trials
 308 in which the class corresponding to 'other' appeared on the screen as either relevant or irrelevant value.

309 For each trial, the three class probabilities sum up to 1 and hence are strongly biased to correlate negatively
 310 with each other. Not surprisingly, we found such strong negative correlations across participants of both pairs of
 311 probabilities, i.e. between P_{EV} and $P_{EV_{back}}$ ($\rho = -.56, \sigma = .22$) as well as between P_{EV} and P_{other} ($\rho = -.40,$
 312 $\sigma = .25$). However, we found that the former correlation was significantly stronger than the latter ($t_{(34)} = -2.77,$
 313 $p = .017$, Fig. 5e), indicating that when the probability assigned to the EV decreased, it was accompanied by a
 314 stronger increase in the probability assigned to EV_{back} , akin to a competition between both types of expectations.
 315 Additionally, a formal model predicting P_{EV} by $P_{EV_{back}}$ resulted in a smaller (i.e. better) AIC (-567.13), compared
 316 to using P_{other} as predictor (-475.32, see online methods). In line with this finding, we turned to test if this
 317 potential competition is reflected in participants' behavior. Of particular relevance in this regard is the behavioral
 318 Congruency effect, which similarly reflects a competition between the different values. Strikingly, we found that
 319 the more negatively P_{EV} correlated with $P_{EV_{back}}$, the stronger Congruency influenced participants' behavior
 320 ($r = -.45, p = .008$, Fig. 5f).

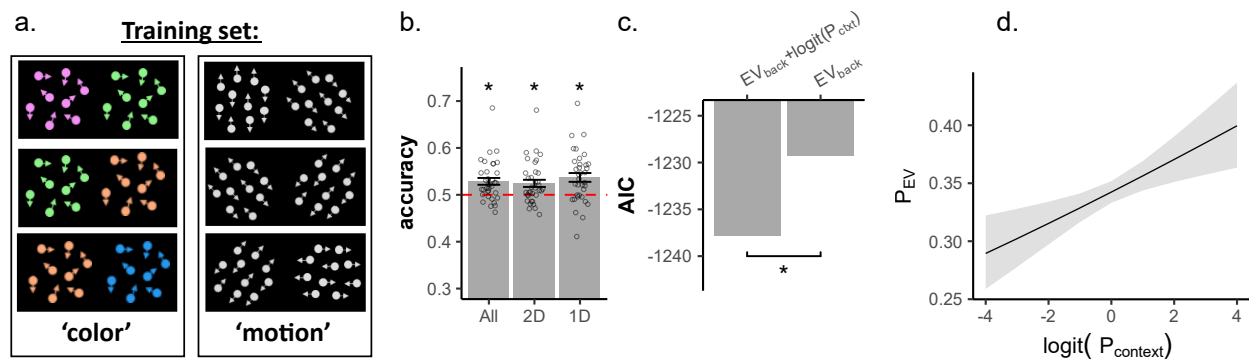


Figure 6: Context decodability in the vmPFC directly relates to the representation of the objective outcome a. We trained the same classifier on the same data only this time we split the training set to classes corresponding to the two possible contexts: Color (left) or Motion (right), irrespective of the EV, though we kept the training sets balanced for EV (see online methods). **b.** The classifier could decode the trial's context above chance also when sub-setting the data to 1D, 2D and when testing on all trials ($p < .001, p = .002, p < .001$, respectively). Error bars represent corrected within subject SEMs [39, 40] c. The trial-context decodability improved prediction of the objective outcome probability, beyond the EV_{back} ($p = .001$). **d.** The objective outcome was strongly represented (P_{EV}), the more the context was decodable from the vmPFC (modeled as logit-transformed probability assigned to the trial-context of the trial, x-axis)

321 In summary, the neural code in vmPFC is mainly influenced by the contextually relevant EV. However, if an
 322 alternative context would lead to a large expected value, the representation of the relevant expected value is
 323 weakened, irrespective of their agreement on the action to be made. Moreover, weakening of the EV representation
 324 is accompanied by a strengthening of the representation of EV_{back} on a trial by trial basis. Lastly, participants
 325 with a stronger influence of high alternative values on the EV representation also had a stronger influence of
 326 EV_{back} on the Congruency RT effect. Likewise, participants who exhibited a larger negative association between
 327 the decodability of EV and the decoded probability of EV_{back} , also reacted slower when the contexts pointed to
 328 different actions. As will be discussed later in detail, we consider this to be evidence for parallel processing of two
 329 task aspects in this region, EV and EV_{back} .

330 **Task-context representations interact with value**
 331 **codes within vmPFC** Above we reported that
 332 vmPFC activity is influenced by multiple value expect-
 333 tations. Which value expectation is currently relevant
 334 depended on the task context. We therefore hypoth-
 335 esized that, in line with previous work, vmPFC would
 336 also encode the task context, although this is not di-
 337 rectly value-related. We thus turned to see if we can
 338 decode the trial's context from the same region that
 339 was univariately sensitive to EV. For this analysis we
 340 trained the same classifier on the same accurate 1D
 341 trials as before, only it was trained to distinguish the
 342 trial types 'Color' and 'Motion' (Fig. 6a). Crucially, the
 343 classifier had no information as to what was the EV of
 344 each given trial, and training sets were up-sampled to
 345 balance the EVs within each set (see online methods).
 346 The classifier was above chance for decoding the correct
 347 context in 1D, 2D and all trials ($t_{(34)} = 3.95, p < .001$,
 348 $t_{(34)} = 3.2, p = .003$, $t_{(34)} = 3.93, p < .001$, respec-
 349 tively, Fig.6b). Additionally, the context is decodable
 350 also when only testing on 2D trials in which value differ-
 351 ence in both contexts was the same (i.e. when keeping
 352 the value difference of the background 20, since the
 353 value difference of the relevant context was always 20,
 354 $t_{(34)} = 2.73, p = .01$).

355 Importantly, if vmPFC is involved in signaling the trial
 356 context as well as the values, then the strength of con-
 357 text signal might relate to the strength of the contextu-
 358 ally relevant value. Strikingly, we found that $P_{context}$
 359 had a positive effect on the decodability of EV and
 360 that adding this term in addition to EV_{back} to the P_{EV}
 361 model improved model fit ($\chi^2_{(1)} = 10.5, p = .001$, Fig. 6c-d). In other words, the more the context was decodable,
 362 the higher was the probability assigned to the correct EV class.

363 Lastly, we investigated how neural representations in vmPFC of EV, EV_{back} and the relevant Context influence
 364 participants' accuracy. Note that the two contexts only indicate different choices in incongruent trials, where a
 365 wrong choice might be a result of a strong influence of the irrelevant context. The behavioral effect on accuracy
 366 could therefore be particularly relevant in this condition. This was also indicated by the analysis of $P_{EV_{back}}$ shown

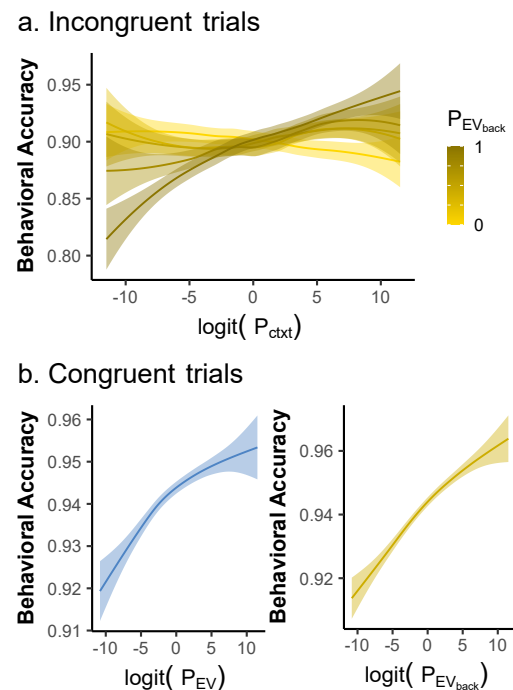


Figure 7: Neural representations of context and value in vmPFC jointly guide behavior **a.** Lower context decodability of the relevant context (x axis) was associated with less behavioral accuracy (y-axis) in incongruent trials ($p = .051$). This effect was modulated by the representation of EV_{back} in vmPFC ($p = .012$, shades of gold), i.e. it was stronger in trials where EV_{back} was strongly decoded from the vmPFC (shades of gold, plotted in 5 quantiles). Shown are fitted slopes from analysis models reported in the text. **b.** Decodability of both EV ($p = .058$, blue, left) and EV_{back} ($p = .009$, gold, right) had a positive relation to behavioral accuracy (y axis) in congruent trials. Shown are fitted slopes from analysis models reported in the text.

in Fig 5d. We therefore modeled congruent and incongruent trials separately. This showed that that a weaker representation of the relevant context was marginally associated with an increased error rate (negative effect of $P_{context}$) on accuracy, LR-test with $P_{context}$: $\chi^2_{(1)} = 3.66, p = .055$). Moreover, if stronger representation of the wrong context (i.e. $1 - P_{context}$) is reducing accuracy, than stronger representation of the value associated with this context (EV_{back}) should strengthen that influence. Indeed, we found that adding a $P_{context} \times P_{EV_{back}}$ term to the model explaining error rates improved model fit ($\chi^2_{(1)} = 6.33, p = .012$, Fig. 7a). Yet, the representation of EV and EV_{back} did not directly influence behavioral accuracy (P_{EV} : $\chi^2_{(1)} = 0.28, p = .599$, $P_{EV_{back}}$: $\chi^2_{(1)} = 0.0, p = .957$). In congruent trials choosing the wrong choice is unlikely a result of wrong context encoding, since both contexts lead to the same choice. Indeed, there was no influence of $P_{context}$ on accuracy for congruent trials (LR-test: $\chi^2_{(1)} = 0.0, p = .922$). However, strong representation of either relevant or irrelevant EV would lead to a correct choice. Indeed, we found that both an increase in $P_{EV_{back}}$ and (marginally) in P_{EV} had a positive relation to behavioral accuracy ($P_{EV_{back}}$: $\chi^2_{(1)} = 6.48, p = .011$, P_{EV} : $\chi^2_{(1)} = 3.5, p = .061$, Fig. 7b).

No evidence for univariate modulation of contextually irrelevant information on expected value signals in vmPFC

The above analyses indicated that multiple value expectations are represented in parallel within vmPFC. Lastly, we asked whether whole-brain univariate analyses could also uncover evidence for processing of multiple value representations. In particular, we asked whether we could find evidence for a single representation that integrates the multiple value expectations into one signal. To this end, we first analyzed the fMRI data using GLMs with separate onsets and EV parametric modulators for 1D and 2D trials (see online methods for details). As expected, several regions were modulated by EV in both trial types, including vmPFC ($EV_{1D} > 0 \cap EV_{2D} > 0$, Fig.8a). Hence, the vmPFC signaled the expected value of the current context in both trial types as expected – even though 2D trials likely required higher attentional demands

(and indeed, the attention network was identified for the $2D > 1D$ contrast, $p < .001$, Fig.8b)

Next, we searched for univariate evidence for processing of irrelevant values by modifying the parametric modulators assigned to 2D trials in the above-mentioned GLM (for full models, see Fig S9). Specifically, in addition to EV_{2D} , we added Congruency (+1 for congruent and -1 for incongruent) and EV_{back} as additional modulators of the activity in 2D trials. This GLM revealed no evidence for a Congruency contrast anywhere in the brain (even at a liberal voxel-wise threshold of $p < .005$), but an unexpected negative effect of EV_{back} in the Superior Temporal Gyrus ($p < .001$, Fig.8c). Notably, unlike the multivariate analysis, no effect in any frontal region was observed. Motivated by our behavioral analysis, we then turned to look for the interaction of each relevant or irrelevant value with Congruency. An analysis including only a Congruency \times EV_{2D} parametric modulator revealed no cluster (even at $p < .005$). Another analysis including Congruency \times EV_{back} in addition to EV_{2D} as parametric

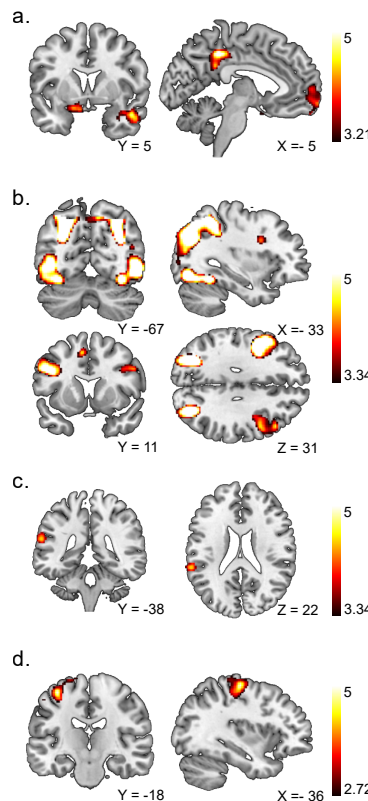


Figure 8: Univariate results Depicted are T-maps for each contrast. A detailed table of clusters can be found in the SI S1. **a.** The intersection of the EV parametric modulators of 1D and 2D trials revealed several regions including right Amygdala, bilateral Hippocampus and Angular Gyrus, the lateral and medial OFC and overlapping vmPFC. Voxelwise threshold $p < .001$, FDR cluster-corrected. **b** 2D trials were characterized by increased activation in an attentional network involving occipital, parietal and frontal clusters ($2D > 1D, p < .001$ FDR cluster corrected). **c.** A region in the Superior Temporal Gyrus was negatively modulated by EV_{back} , i.e. the higher the EV_{back} , the lower the signal in this region. $p < .001$, FDR cluster-corrected. No overlap with (b), see S9. **d.** A cluster in the primary motor cortex was negatively modulated by Congruency \times EV_{back} , i.e. the difference between Incongruent and Congruent trials increased with higher EV_{back} , similar to the RT effect, $p < .005$, FDR cluster-corrected. No overlap with (b), see S9

413 modulators, however, revealed a negative effect in the primary motor cortex at a liberal threshold, which indicated
414 that the difference between Incongruent and Congruent trials increased with higher EV_{back} , akin to a response
415 conflict ($p < .005$, Fig.8d). Lastly, we re-ran all above analyses concerning Congruency and EV_{back} only inside
416 the identified vmPFC ROI. No voxel survived for Congruency, EV_{back} nor the interactions, even at threshold of
417 $p < .005$.

418 Additional exploratory analyses such as contrasting the onsets of congruent and incongruent trials, confirmed the
419 lack of Congruency modulation in any frontal region (Fig. S9). Interestingly, at a liberal threshold of $p < .005$
420 we found stronger activity for 1D over 2D trials in a cluster overlapping with vmPFC ($1D > 2D$, $p < .005$, S9).
421 Although this could be interpreted as a general preference for 1D trials, splitting the 2D onsets by Congruency
422 revealed no cluster for $1D > Incongruent$ (also at $p < .005$) but a stronger cluster for $1D > Congruent$ ($p < .001$, Fig.
423 S9). In other words, the signal in the vmPFC was *weaker* when both contexts indicate the same action, compared
424 to when only one context is present.

425 In summary, our univariate analyses indicated the well-known sensitivity of vmPFC to values expected within the
426 relevant context. Yet, unlike our multivariate analyses, we found no evidence for signal modulation by contextually
427 irrelevant values outside the motor cortex, where we found a negative modulation of Congruency $\times EV_{back}$. This
428 contrasts with the idea that competing values would have been integrated into a single EV representation in the
429 vmPFC, because this account would have predicted a higher signal for Congruent compared to Incongruent trials.
430 If at all, we found a general decrease in signal for Congruent trials.

431 Discussion

432 In this study, we investigated how contextually-irrelevant value expectations influence behavior as well as neural
433 vmPFC activation patterns. We asked participants to make choices between options that had different expected
434 values in different task-contexts. Participants reacted slower when the expected values in the irrelevant context
435 favored a different choice, compared to trials in which relevant and irrelevant contexts favored the same choice.
436 This Congruency effect increased with increasing reward associated with the hypothetical choice in the irrelevant
437 context (EV_{back}). We then identified a functional ROI that is univariately sensitive to the objective expected
438 values (EV), i.e. the contextually-relevant rewards. Multivariate analyses revealed that a high EV_{back} disrupts
439 the value-code of the vmPFC. Specifically, higher EV_{back} was associated with a degraded representation of the
440 objective EV (P_{EV}) in vmPFC. At the same time, increased representation of EV_{back} in the vmPFC during stimuli
441 presentation was associated with an increased chance of choosing accordingly, irrespective of its agreement with
442 the relevant context. Moreover, the decrease in decodability of the value in the relevant context was associated
443 with an increase in the value that would be obtained in the other task-context ($P_{EV_{back}}$), akin to a conflict of
444 the two value representations. Both these effects were associated with the congruency-related behavioral slowing.
445 Importantly, we also found that the task context (color/motion) could be decoded from the same brain region.
446 This decodability of the context was related to the decodability of the value in the current context. Lastly, we are
447 aware that in binary decoding, low decodability of the correct class doesn't necessarily point to high decodability
448 of the alternative class. Nevertheless, when the irrelevant context pointed to the wrong choice in incongruent
449 trials, stronger vmPFC representation of the alternative (wrong) context and its corresponding value were related
450 to higher error rates. However, when both contexts agreed on the action to be made, stronger representation of
451 either of their EVs were strongly related to making a correct choice.

452 We found no evidence that the signal in vmPFC is sensitive to Congruency. The only region that was univariately
453 modulated by Congruency was the primary motor cortex. These data suggest a complex multi-faceted value
454 representation in vmPFC, in which multiple values of the same option under different task-contexts are reflected
455 and influence behavior. While we could not directly decode EV_{back} , it had a significant and value-dependent effect
456 on EV representations, hinting at a complex form of co-representation within the vmPFC. Moreover, we could also

457 decode the current task-context from vmPFC, and the strength of context encoding is related to the strength of
458 the representation of the context associated value.

459 Behavioral analyses showed outcome-irrelevant values are not completely filtered. In our experiment the relevant
460 features were cued explicitly and the rewards were never influenced by the irrelevant features. Nevertheless,
461 participants' reactions were influenced by not only the contextually relevant outcome, but also the counterfactual
462 choice, based on values irrelevant in the given context. These results raise the question how internal value
463 expectation(s) of the choice are shaped by the possible contexts. One hypothesis could be that rewards expected
464 in both contexts integrate into a single EV for a choice, which in turn guides behavior. This perspective suggests
465 that the expected value of options valuable in both contexts will increase, relative to options that are valuable only
466 in the current but not in the alternative context. In other words, in trials in which the irrelevant context agreed
467 with the decision, the (subjective) EV of choice might increase, in proportion to how large the irrelevant value was.
468 However, if the alternative context disagrees, the (subjective) EV might decrease. This approach would treat RT
469 as a direct measure of EV.

470 An alternative hypothesis would be that both values are kept separate, and will be processed in parallel. In this case,
471 their conflict would have to be resolved in a different brain region, such as the motor cortex. This would suggest
472 that behavior is guided by two value expectations that are resolved into action, likely outside the value-network.
473 To differentiate these possibilities motivated us to focus our analysis on the vmPFC, where we could distinguish
474 between a single integrated value and simultaneously oc-occurring representations. Notably, the interaction of
475 values could be also influenced by a representation of the current task context, which is known to be represented in
476 the same region and the overlapping orbitofrontal cortex [e.g., 32, 34, 35, 45]. It therefore seemed to be a good
477 candidate region to help illuminate how values stemming from different contexts, as well as information about the
478 contexts themselves, might interact in the brain.

479 The lack of a Congruency effect on univariate vmPFC signals contradicted the integration hypothesis. Even
480 before considering the specific outcomes of the two contexts, it would predict an increased signal for congruent
481 compared to incongruent trials. If at all, we find the univariate vmPFC activation in 1D trials to be stronger than
482 in Congruent 2D trials.

483 Interestingly, the univariate analysis was not sensitive enough to detect an influence of the irrelevant values in
484 vmPFC. Only an investigation into the multivariate analyses revealed a degraded EV representation in trials with
485 stronger alternative values, suggesting that the two potential values are in representational conflict. This impact
486 on value representations occurred irrespective of choice congruency, but correlated with the behavioral modulation
487 of EV_{back} on congruency. Due to limitations of our design, we could not successfully train a classifier directly
488 on EV_{back} of 2D trials. Moreover, the objective class was not strongly represented when both expected values
489 (EV and EV_{back}) were the same, suggesting some differences in the underlying representations of relevant and
490 irrelevant values. However, a classifier trained on EV in 1D trials in which no irrelevant values were present, was
491 still sensitive to the expected value of the irrelevant context in 2D trials. This could suggest that within the vmPFC
492 'conventional' expected values and counterfactual values are encoded using at least partially similar patterns.

493 This interpretation would also be supported by our findings that both representations contributed to choice
494 accuracy in Congruent trials, and that $P_{EV_{\text{back}}}$ and P_{EV} were negatively correlated, such that decreases in the EV
495 representation were accompanied by an increased EV_{back} representation. This might also explain how the reducing
496 effect EV_{back} had on the EV representation aligns well with behavioral changes observed in incongruent trials (i.e.
497 reducing both RT and accuracy), but also our finding of improved performance on congruent trials, even though
498 there EV_{back} could still be large: in the first case, when choices for the two context differ, competing EV and
499 EV_{back} lead to performance decrements; in the second case, when choices are the same, both of the independently
500 contributing representations would support the same reaction and therefore benefit performance. Our results

501 therefore are in line with the interpretation that both relevant and irrelevant values are retrieved, represented in
502 parallel within the vmPFC and influence behavior.

503 At the same time, our results also suggest that while the EV_{back} influenced the representation of EV, the latter
504 largely dominated population activity. This is in line with our task requirements and participant's high behavioral
505 accuracy that indicated accurate choices were driven by EV in the vast majority of cases. However, even when
506 focusing only on behavioral accurate trials, we see that the signal in vmPFC encompass a representational conflict
507 between the two EVs, which was related to Congruency-dependent RT effects in those trials. Interestingly,
508 univariate analyses were not sensitive enough to detect an influence of the outcome-irrelevant values in the vmPFC.

509 Univariate analyses revealed a weak negative modulation of primary motor cortex activity by Congruency. Akin
510 to a response conflict, this corresponds to recent findings that distracting information can be traced to areas
511 involved in task execution cortex in humans and monkeys [21, 22]. Crucially however, unlike in previous studies the
512 modulation found in our study was dependent on the specific values of the alternative context. This could suggest
513 that the outcome-representation conflict in the vmPFC is resolved in the primary motor cortex. This would also be
514 in line with our interpretation that the vmPFC does not integrate both tasks into a single EV representation.

515 One important implication of our study concerns the nature of neural representations in the vmPFC/mOFC. A
516 pure perceptual representation should be equally influenced by all four features on the screen. Yet, our decoding
517 results could not have been driven by the perceptual properties of the chosen feature, and effects of background
518 values could also not be explained by perceptual features of the ignored context (Fig. 3 and Fig. S7). Moreover,
519 we show that the signal in vmPFC reflects more than expected values of the choice, and we did not find any
520 evidence for value integration. Finally, investigating trials on which both expected values, EV and EV_{back} , were
521 the same, we did not find a stronger signal for the objective class. This indicates that our classifier was neither
522 exclusively sensitive to the perceptual features, nor to values regardless of whether they were relevant or not. Both
523 those accounts would predict an increased representation of the objective class in those trials. Instead, we show
524 that vmPFC simultaneously represents option values as well as information about the current task-context, and
525 that both these representations interact with each other as well as behavior. One possible solution which has
526 been suggested in previous research is that vmPFC/mOFC might be tasked with representing a task-state, which
527 effectively encodes the current state of all information relevant to the task, in particular if information is partially
528 observable [32, 45]. Note that the task context, which we decode from vmPFC activity in the present paper, could
529 be considered as a superset of the more fine grained task states that reflect the individual motion directions/colors
530 involved in a comparison. Any area sensitive to these states would therefore also show decoding of context as
531 defined here. Whether vmPFC has access to such detailed information about the states cannot be conclusively
532 answered with the present research for power reasons.

533 Of note, some work has found that EV could be one additional aspect of OFC activity [36] that is multiplexed
534 with other task-related information. Crucially, the idea of task-state as integration of task-relevant information
535 [28, 46] could explain why this region was found crucial for integrating valued features, when all features of an
536 object are relevant for choice [16, 28], although some work suggests that it might even reflect features not carrying
537 any value [29]. Moreover, the link between context and EV decodability as well as to behavioral accuracy suggests
538 a multi-faceted vmPFC representation which not only contains multiple values, but also links information about
539 the relevant task context to the corresponding values, just as the task-state framework might suggest.

540 To conclude, the main contribution of our study is that we elucidated the relation between task-context and value
541 representations within the vmPFC. By introducing multiple possible values of the same option in different contexts,
542 we were able to reveal a complex representation of task structure in vmPFC, with both task-contexts and their
543 associated values activated in parallel. The decodability of both context and value(s) independently from vmPFC,
544 and their relation to choice behavior, hints at integrated computation of these in this region. We believe that this
545 bridges between findings of EV representation in this region to the functional role of this region as representing

546 task-states, whereby relevant and counterfactual values can be considered as part of a more encompassing state
547 representation.

548 **Acknowledgments**

549 NWS was funded by an Independent Max Planck Research Group grant awarded by the Max Planck Society
550 (M.TN.A.BILD0004) and a Starting Grant from the European Union (ERC-2019-StG REPLAY-852669). NM
551 was funded by and is grateful for a scholarship from the Ernst Ludwig Ehrlich Studienwerk (ELES) and Einstein
552 Center for Neuroscience (ECN) Berlin throughout this study. We thank Gregor Caregnato for help with participant
553 recruitment, Anika Löwe, Lena Maria Krippner, Sonali Beckmann and Nadine Taube for help with data acquisition,
554 all participants for their participation and the Neurocode lab for numerous contributions and help throughout this
555 project.

556 **Data availability statement**

557 The MRI data that support the findings of this study will be made available upon publication.

558 **Code availability statement**

559 Custom code for all analyses conducted in this study will be made available upon publication.

560 Online Methods

561 Participants

562 Forty right-handed young adults took part in the experiment (18 women, $\mu_{age} = 27.6, \sigma_{age} = 3.35$) in exchange
563 for monetary reimbursement. Participants were recruited using the participant database of Max-Planck-Institute
564 for Human Development. Beyond common MRI-safety related exclusion criteria (e.g. piercings, pregnancy, large or
565 circular tattoos etc.), we also did not admit participants to the study if they reported any history of neurological
566 disorders, tendency for back pain, color perception deficiencies or if they had a head circumference larger than 58
567 cm (due to the limited size of the 32-channel head-coil). After data acquisition, we excluded five participants from
568 the analysis; one for severe signal drop in the OFC, i.e. more than 15% less voxels in functional data compared to
569 the OFC mask extracted from freesurfer parcellation of the T1 image [47, 48]. One participant was excluded due
570 to excessive motion during fMRI scanning (more than 2mm in any axial direction) and three participants for low
571 performance (less than 75% accuracy in one context in the main task). In the behavioral-replication, 23 young
572 adults took part (15 women, $\mu_{age} = 27.1, \sigma_{age} = 4.91$) and two were excluded for the same accuracy threshold.
573 Due to technical reasons, 3 trials (4 in the replication sample) were excluded since answers were recorded before
574 stimulus was presented and 2 trials (non in the replication) in which RT was faster than 3 SD from the mean
575 (likely premature response). The monetary reimbursement consisted of a base payment of 10 Euro per hour (8.5
576 for replication sample) plus a performance dependent bonus of 5 Euro on average. The study was approved the
577 the ethics board of the Free University Berlin (Ref. Number: 218/2018).

578 Experimental procedures

579 **Design** Participants performed a random dot-motion paradigm in two phases, separated by a short break
580 (minimum 15 minutes). In the first phase, psychophysical properties of four colors and four motion directions were
581 first titrated using a *staircasing task*. Then, participants learned the rewards associated with each of these eight
582 features during a *outcome learning task*. The second phase took place in the MRI scanner and consisted mainly of
583 the *main task*, in which participants were asked to make decisions between two random dot kinematograms, each
584 of which had one color and/or one direction from the same set. Note there were two additional mini-blocks of 1D
585 trials only, at the end of first- and at the start of the second phase (during anatomical scan, see below). The
586 replication sample completed the same procedure with the same break length, but without MRI scanning. That is,
587 both phases were completed in a behavioral testing room. Details of each task and the stimuli are described below.
588 Behavioral data was recorded during all experiment phases. MRI data was recorded during phase 2. We additionally
589 collected eye-tracking data (EyeLink 1000; SR Research Ltd.; Ottawa, Canada) both during the staircasing and
590 the main decision making task to ensure continued fixation (data not presented). The overall experiment lasted
591 XXX minutes on average.

592 **Room, Luminance and Apparatus** Behavioral sessions were conducted in a dimly lit room without natural
593 light sources, such that light fluctuations could not influence the perception of the features. A small lamp was
594 stationed in the corner of the room, positioned so it would not cast shadows on the screen. The lamp had a light
595 bulb with 100% color rendering index, i.e. avoiding any influence on color perception. Participants sat on a height
596 adjustable chair at a distance of 60 cm from a 52 cm horizontally wide, Dell monitor (resolution: 1920 × 1200,
597 refresh rate 1/60 frames per second). Distance from the monitor was fixed using a chin-rest with a head-bar.
598 Stimuli were presented using psychtoolbox version 3.0.11 [49–51] in MATLAB R2017b [52] In the MRI-scanner
599 room lights were switched off and light sources in the operating room were covered in order to prevent interference
600 with color perception or shadows cast on the screen. Participants lay inside the scanner at distance of 91 cm from
601 a 27 cm horizontally wide screen on which the task was presented a D-ILA JVC projector (D-ILa Projektor SXGA,

602 resolution: 1024x768 , refresh rate: 1/60 frames per second). Stimuli were presented using psychtoolbox version
603 3.0.11 [49–51] in MATLAB R2012b [53] on a Dell precision T3500 computer running windows XP version 2002.

604 **Stimuli** Each cloud of dots was presented on the screen in a circular array with 7° visual angle in diameter. In
605 all trials involving two clouds, the clouds appeared with 4° visual angle distance between them, including a fixation
606 circle (2° diameter) in the middle, resulting in a total of 18° field of view [following total apparatus size from 38].
607 Each cloud consisted of 48 square dots of 3×3 pixels. We used four specific motion and four specific color features.

608 To prevent any bias resulting from the correspondence between response side and dot motion, each of the four
609 motion features was constructed of two angular directions rotated by 180° , such that motion features reflected an
610 axis of motion, rather than a direction. Specifically, we used the four combinations: 0° - 180° (left-right), 45° - 225°
611 (bottom right to upper left), 90° - 270° (up-down) and 135° - 315° (bottom left - upper right). We used a Brownian
612 motion algorithm [e.g. 38], meaning in each frame a different set of given amount of coherent dots was chosen
613 to move coherently in the designated directions in a fixed speed, while the remaining dots moved in a random
614 direction (Fig. S1). Dots speed was set to 5° per second [i.e. $2/3$ of the aperture diameter per second, following
615 38]. Dots lifetime was not limited. When a dot reached the end of the aperture space, it was sent 'back to start',
616 i.e. back to the other end of the aperture. Crucially, the number of coherent dots (henceforth: motion-coherence)
617 was adjusted for each participant throughout the staircasing procedure, starting at 0.7 to ensure high accuracy [see
618 38]. An additional type of motion-direction was 'random-motion' and was used in 1D color clouds. In these clouds,
619 dots were split to 4 groups of 12, each assigned with one of the four motion features and their adjusted-coherence
620 level, resulting in a balanced subject-specific representation of random motion.

621 In order to keep the luminance fixed, all colors presented in the experiment were taken from the YCbCr color
622 space with a fixed luminance of $Y = 0.5$. YCbCr is believed to represent human perception in a relatively accurate
623 manner [cf. 54]. In order to generate an adjustable parameter for the purpose of staircasing, we simulated a
624 squared slice of the space for $Y = 0.5$ (Fig. S1) in which the representation of the dots color moved using a
625 Brownian motion algorithm as well. Specifically, all dots started close to the (gray) middle of the color space, in
626 each frame a different set of 30% of dots was chosen to move coherently towards the target color in a certain
627 speed whereas all the rest were assigned with a random direction. Perceptually, this resulted in all the dots being
628 gray at the start of the trial and slowly taking on the designated color. Starting point for each color was chosen
629 based on pilot studies and was set to a distance of 0.03-0.05 units in color space from the middle. Initial speed in
630 color space (henceforth: color-speed) was set so the dots arrive to their target (23.75% the distance to the corner
631 from the center) by the end of the stimulus presentation (1.6s). i.e. distance to target divided by the number of
632 frames per trial duration. Color-speed was adjusted throughout the staircasing procedure. An additional type of
633 color was 'no color' for motion 1D trials for which we used the gray middle of the color space.

634 **Staircasing task** In order to ensure RTs mainly depended on associated values and not on other stimulus
635 properties (e.g. salience), we created a staircasing procedure that was conducted *prior to value learning*. In this
636 procedure, motion-coherence and color-speed were adjusted for each participant in order to minimize between-
637 feature detection time differences. As can be seen in Fig. S1, in this perceptual detection task participants were
638 cued (0.5s) with either a small arrow (length 2°) or a small colored circle (0.5° diameter) to indicate which
639 motion-direction or color they should choose in the upcoming decision. After a short gray (middle of YCbCr)
640 fixation circle (1.5s, diameter 0.5°), participants made a decision between the two clouds (1.6s). Clouds in this part
641 could be either both single-feature or both dual-features. In dual feature trials, each stimulus had one color and
642 one motion feature, but the cue indicated either a specific motion or a specific color. After a choice, participants
643 received feedback (0.4s) whether they were (a) correct and faster than 1 second, (b) correct and slower or (c)
644 wrong. After a short fixation (0.4s), another trial started. All timings were fixed in this part. Participants were
645 instructed to always look at the fixation circle in the middle of the screen throughout this and all subsequent tasks.
646 To motivate participants and continued perceptual improvements during the later (reward related) task-stages,

647 participants were told that if they were correct and faster than 1 second in at least 80% of the trials, they will
648 receive an additional monetary bonus of 2 Euros.

649 The staircasing started after a short training (choosing correct in 8 out of 12 consecutive trials mixed of both
650 contexts) and consisted of two parts: two *adjustment blocks* and two *measurement blocks*. All adjustments of
651 color-speed and motion-coherence followed this formula:

$$\theta_i^{t+1} = \theta_i^t + \alpha \theta_i^t \frac{\overline{RT}_i^t - RT^0}{RT^0} \quad (1)$$

652 where θ_i^{t+1} represents the new coherence/speed for motion or color feature i during the upcoming time interval/block
653 $t + 1$, θ_i^t is the level at the time of adjustment, \overline{RT}_i^t is the mean RT for the specific feature i during time interval
654 t , RT^0 is the “anchor” RT towards which the adjustment is made and α represents a step size of the adjustment,
655 which changed over time as described below.

656 The basic building block of *adjustment blocks* consisted of 24 cued-feature choices for each context ($4 \times 3 \times$
657 $2 = 24$, i.e. 4 colors, each discriminated against 3 other colors, on 2 sides of screen). The same feature was
658 not cued more than twice in a row. Due to time constraints, we could not include all possible feature-pairing
659 combinations between the cued and uncued features. We therefore pseudo-randomly choose from all possible
660 background combinations for each feature choice (unlike later stages, this procedure was validated on and therefore
661 included also trials with identical background features). In the first adjustment block, participants completed 72
662 trials, i.e. 36 color-cued and 36 motion-cued, interleaved in chunks of 4-6 trials in a non-predictive manner. This
663 included, for each context, a mixture of one building block of 2D trials and half a block of 1D trials, balanced
664 to include 3 trials for each cued-feature. 1D or 2D trials did not repeat more than 3 times in a row. At the end
665 of the first adjustment block, the mean RT of the last 48 (accurate) trials was taken as the anchor (RT^0) and
666 each individual feature was adjusted using the above formula with $\alpha = 1$. The second adjustment block started
667 with 24 motion-cued only trials which were used to compute a new anchor. Then, throughout a series of 144
668 trials (72 motion-cued followed by 72 color-cued trials, all 2D), every three correct answers for the same feature
669 resulted in an adjustment step for that specific feature (Eq. 1) using the average RT of these trials (\overline{RT}_i^t) and the
670 motion anchor RT^0 for both contexts. This resulted in a maximum of six adjustment steps per feature, where
671 alpha decreased from 0.6 to 0.1 in steps of 0.1 to prevent over-adjustment.

672 Next, participants completed two *measurement blocks* identical in structure to the main task (see below) with two
673 exceptions: First, although this was prior to learning the values, they were perceptually cued to choose the feature
674 that later would be assigned with the highest value. Second, to keep the relevance of the feature that later would
675 take the lowest value (i.e. would rarely be chosen), we added 36 additional trials cued to choose that feature (18
676 motion and 18 color trials per block).

677 **Outcome learning task** After the staircasing and prior to the main task, participants learned to associate each
678 feature with a deterministic outcome. Outcomes associated with the four features on each contexts were 10, 30,
679 50 and 70 credit-points. The value mapping to perceptual features was assigned randomly between participants,
680 such that all possible color- and all possible motion-combinations were used at least once ($4! = 24$ combinations
681 per context). We excluded motion value-mapping that correspond to clockwise or counter-clockwise ordering. The
682 outcome learning task consisted only of single-feature clouds, i.e. clouds without coherent motion or dots ‘without’
683 color (gray). Therefore each cloud in this part only represented a single feature. To encourage mapping of the
684 values for each context on similar scales, the two clouds could be either of the same context (e.g. color and color)
685 or from different contexts (e.g. color and motion). Such context-mixed trials did not repeat in other parts of the
686 experiment.

687 The first block of the outcome learning task had 80 *forced choice* trials (5 repetitions of 16 trials: 4 values \times 2
688 Context \times 2 sides of screen), in which only one cloud was presented, but participants still had to choose it to

689 observe its associated reward. These were followed by mixed blocks of 72 trials which included 16 *forced choice*
690 interleaved with 48 *free choice* trials between two 1D clouds (6 value-choices: 10 vs 30/50/70, 30 vs 50/70, 50
691 vs 70 × 4 context combinations × 2 sides of screen for highest value). To balance the frequencies with which
692 feature-outcome pairs would be chosen, we added 8 forced choice trials in which choosing the lowest value was
693 required. Trials were pseudo-randomized so no value would repeat more than 3 times on the same side and same
694 side would not be chosen more the three consecutive times. Mixed blocks repeated until participants reached at
695 least 85% accuracy of choosing the higher valued cloud in a block, with a minimum of two and a maximum of
696 four blocks. Since all clouds were 1D and choice could be between contexts, these trials started without a cue,
697 directly with the presentation of two 1D clouds (1.6s). Participants then made a choice, and after short fixation
698 (0.2s) were presented with the value of both chosen and unchosen clouds (0.4s, with value of choice marked with
699 a square around it, see Fig. S1). After another short fixation (0.4s) the next trial started. Participants did not
700 collect reward points in this stage, but were told that better learning of the associations will result in more points,
701 and therefore more money later. Specifically, in the MRI experiment participants were instructed that credit points
702 during the main task will be converted into a monetary bonus such that every 600 points they will receive 1 Euro
703 at the end. The behavioral replication cohort received 1 Euro for every 850 points.

704 **Main task preparation** In preparation of the main task, participants performed one block of 1D trials at the
705 end of phase 1 and then at the start of the MRI session during the anatomical scan. These blocks were included to
706 validate that changing presentation mediums between phases (computer screen versus projector) did not introduce
707 a perceptual bias to any features and as a final correction for post value-learning RT differences between contexts.
708 Each block consisted of 30 color and 30 motion 1D trials interleaved in chunks of 4-7 trials in a non-predictive
709 manner. The value difference between the clouds was fixed to 20 points (10 repetitions of 3 value comparisons ×
710 2 contexts). Trials were pseudo-randomized so no target value was repeated more than once within context (i.e.
711 not more than twice all in all) and was not presented on the same side of screen more than 3 consecutive trials
712 within context and 4 in total. In each trial, they were first presented with a contextual cue (0.6s) for the trial,
713 followed by short fixation (0.5s) and the presentation of two single-feature clouds of the cued context (1.6s) and
714 had to choose the highest valued cloud. After a short fixation (0.4s), participants were presented with the chosen
715 cloud's outcome (0.4s). The timing of the trials was fixed and shorter than in the remaining main task because no
716 functional MRI data was acquired during these blocks. Participants were instructed that from the first preparation
717 block they started to collect the rewards. Data from these 1D block were used to inspect and adjust for potential
718 differences between the MRI and the behavior setup. First, participants reacted generally slower in the scanner
719 ($t(239) = -9.415, p < .001$, paired t-test per subject per feature). Importantly, however, we confirmed that this
720 slowing was uniform across features, i.e. no evidence was found for a specific feature having more RT increase
721 than the rest (ANOVA test on the difference between the phases, $F(7, 232) = 1.007, p = .427$). Second, because
722 pilot data indicated increased RT differences between contexts after the outcome learning task we took the mean
723 RT difference between color and motion trials in the second mini-block in units of frames (RT difference divided by
724 the refresh rate), and moved the starting point of each color relative to their target color, the number of frames ×
725 its speed. Crucially, the direction of the move (closer/further to target) was the same for all colors, thus ensuring
726 not to induce within-context RT differences.

727 **Main task** Finally, participants began with the main experiment inside the scanner. Participants were asked to
728 choose the higher-valued of two simultaneously presented random dot kinematograms, based on the previously
729 learned feature-outcome associations. As described in the main text, each trial started with a cue that indicated
730 the current task context (color or motion). In addition, both clouds could either have two features (each a color
731 and a motion, *2D trials*) or one feature only from the cued context (e.g., colored, but randomly moving dots).

732 The main task consisted of four blocks in which 1D and 2D trial were intermixed. Each block contained 36 1D
733 trials (3 EV × 2 Contexts × 6 repetitions) and 72 2D trials (3 EV × 2 Contexts × 12 feature-combinations, see

734 fig1c). Since this task took part in the MRI, the duration of the fixation circles were drawn from an truncated
735 exponential distribution with a mean of $\mu=0.6s$ (range 0.5s-2.5s) for the interval between cue and stimulus, a
736 mean of $\mu=3.4s$ (1.5s-9s) for the interval between stimulus and outcome and a mean of $\mu=1.25s$ (0.7s-6s) for
737 the interval between outcome and the cue of the next trial. The cue, stimulus and outcome were presented for
738 0.6s, 1.6s and 0.8s, respectively. Timing was optimized using VIF-calculations of trial-wise regression models (see
739 Classification procedure section below).

740 The order of trials within blocks was controlled as follows: the cued context stayed the same for 4-7 trials (in a
741 non-predictive manner), to prevent context confusion caused by frequent switching. No more than 3 repetitions of
742 1D or 2D trials within each context could occur, and no more than 5 repetition overall. The target did not appear
743 on the same side of the screen on more than 4 consecutive trials. Congruent or incongruent trials did not repeat
744 more than 3 times in a row. In order to avoid repetition suppression, i.e. a decrease in the fMRI signal due to a
745 repetition of information [e.g. 55, 56], no target feature was repeated two trials in a row, meaning the EV could
746 repeat maximum once (i.e. one color and one motion). As an additional control over repetition, we generated
747 1000 designs according the above-mentioned rules and choose the designs in which the target value was repeated
748 in no more than 10% of trials across trial types, as well as when considering congruent, incongruent or 1D trials
749 separately.

750 Behavioral analysis

751 RT data was analyzed in R (R version 3.6.3 [57], RStudio version 1.3.959 [58]) using linear mixed effect models
752 (lmer in lme4 1.1-21: [59]). When describing main effects of models, the χ^2 represents Type II Wald χ^2 tests,
753 whereas when describing model comparison, the χ^2 represents the log-likelihood ratio test. Model comparison
754 throughout the paper was done using the 'anova' function. Regressors were scaled prior to fitting the models for
755 all analyses. The behavioral model that we found to fit the behavioral RT data best was:

$$\log RT_k^t = \beta_0 + \gamma_{0k} + \beta_1 EV + \beta_2 Congruency_t + \beta_3 Congruency_t \times EV_{back_t} + \beta_4 Congruency_t \times EV_t + \nu_1 t + \nu_2 side_t + \nu_3 switch_t + \nu_4 context_t \quad (2)$$

756 where $\log RT_k^t$ is the log reaction time of subject k in trial t , β_0 and γ_{0k} represent global and subject-specific
757 intercepts, ν -coefficients reflect nuisance regressors ($side$ of target object, trials since last context $switch$ and the
758 current $context$), β_1 to β_4 captured the fixed effect of EV, Congruency, Congruency \times EV_{back} and Congruency \times
759 EV, respectively. The additional models reported in the SI included intercept terms specific for each factor level,
760 nested within subject (for EV, Block and Context, see Fig. S2). Investigations of alternative parametrizations of
761 the values can be found in Fig. S3.

762 Accuracy data was analyzed in R (R version 3.6.3 [57], RStudio version 1.3.959 [58]) using generalized linear mixed
763 effect models (glmer in lme4 1.1-21: [59]) employing a binomial distribution family with a 'logit' link function.
764 Regressors were scaled prior to fitting the models for all analyses. No-answer trials were excluded from this
765 analysis. The model found to fit the behavioral accuracy data best was almost equivalent to the RT model, except
766 for the fourth term involving Congruency \times switch:

$$ACC_k^t = \beta_0 + \gamma_{0k} + \beta_1 EV + \beta_2 Congruency_t + \beta_3 Congruency_t \times EV_{back_t} + \beta_4 Congruency_t \times switch_t + \nu_1 t + \nu_2 side_t + \nu_3 switch_t + \nu_4 context_t \quad (3)$$

767 where ACC_k^t is the accuracy (1 for correct and 0 for incorrect) of subject k in trial t and all the rest of the
768 regressors are equivalent to Eq. 2. We note that the interaction Congruency \times switch indicates that participants
769 were more accurate the further they were from a context switch point.

770 **fMRI data**

771 **fMRI data acquisition** MRI data was acquired using a 32-channel head coil on a research-dedicated 3-Tesla
772 Siemens Magnetom TrioTim MRI scanner (Siemens, Erlangen, Germany) located at the Max Planck Institute for
773 Human Development in Berlin, Germany. High-resolution T1-weighted (T1w) anatomical Magnetization Prepared
774 Rapid Gradient Echo (MPRAGE) sequences were obtained from each participant to allow registration and brain
775 surface reconstruction (sequence specification: 256 slices; TR = 1900 ms; TE = 2.52 ms; FA = 9 degrees;
776 inversion time (TI) = 900 ms; matrix size = 192 \times 256; FOV = 192 \times 256 mm; voxel size = 1 \times 1 \times 1 mm).
777 This was followed with two short acquisitions with six volumes each that were collected using the same sequence
778 parameters as for the functional scans but with varying phase encoding polarities, resulting in pairs of images
779 with distortions going in opposite directions between the two acquisitions (also known as the blip-up / blip-down
780 technique). From these pairs the displacements were estimated and used to correct for geometric distortions due to
781 susceptibility-induced field inhomogeneities as implemented in the the fMRIPrep preprocessing pipeline. In addition,
782 a whole-brain spoiled gradient recalled (GR) field map with dual echo-time images (sequence specification: 36
783 slices; A-P phase encoding direction; TR = 400 ms; TE1 = 4.92 ms; TE2 = 7.38 ms; FA = 60 degrees; matrix
784 size = 64 \times 64; 619 FOV = 192 \times 192 mm; voxel size = 3 \times 3 \times 3.75 mm) was obtained as a potential alternative
785 to the method described above. However, this GR field map was not used in the preprocessing pipeline. Lastly,
786 four functional runs using a multi-band sequence (sequence specification: 64 slices in interleaved ascending order;
787 anterior-to-posterior (A-P) phase encoding direction; TR = 1250 ms; echo time (TE) = 26 ms; voxel size = 2 \times 2
788 \times 2 mm; matrix = 96 \times 96; field of view (FOV) = 192 \times 192 mm; flip angle (FA) = 71 degrees; distance factor =
789 0, MB acceleration factor = 4). A tilt angle of 30 degrees from AC-PC was used in order to maximize signal from
790 the orbitofrontal cortex (OFC, see [60]). For each functional run, the task began after the acquisition of the first
791 four volumes (i.e., after 5.00 s) to avoid partial saturation effects and allow for scanner equilibrium. Each run was
792 about 15 minutes in length, including a 20 seconds break in the middle of the block (while the scanner is running)
793 to allow participants a short break. We measured respiration and pulse during each scanning session using pulse
794 oximetry and a pneumatic respiration belt part of the Siemens Physiological Measurement Unit.

795 **BIDS conversion and defacing** Data was arranged according to the brain imaging data structure (BIDS) specifi-
796 cation [61] using the HeuDiConv tool (version 0.6.0.dev1; freely available from <https://github.com/nipy/heudiconv>).
797 DicomS were converted to the NIfTI-1 format using dcm2niix [version 1.0.20190410 GCC6.3.0; [62]]. In order
798 to make identification of study participants highly unlikely, we eliminated facial features from all high-resolution
799 structural images using pydeface (version 2.0; available from <https://github.com/poldracklab/pydeface>). The data
800 quality of all functional and structural acquisitions were evaluated using the automated quality assessment tool
801 MRIQC [for details, [see 63], and the MRIQC documentation]. The visual group-level reports confirmed that the
802 overall MRI signal quality was consistent across participants and runs.

803 **fMRI preprocessing** Data was preprocessed using *fMRIPrep* 1.2.6 (Esteban et al. [64]; Esteban et al.
804 [65]; RRID:SCR_016216), which is based on *Nipype* 1.1.7 (Gorgolewski et al. [66]; Gorgolewski et al. [67];
805 RRID:SCR_002502). Many internal operations of *fMRIPrep* use *Nilearn* 0.5.0 [68, RRID:SCR_001362], mostly
806 within the functional processing workflow.

807 Specifically, the T1-weighted (T1w) image was corrected for intensity non-uniformity (INU) using
808 *N4BiasFieldCorrection* [69, ANTs 2.2.0], and used as a T1w-reference throughout the workflow. The anatomi-
809 cal image was skull-stripped using *antsBrainExtraction.sh* (ANTs 2.2.0), using OASIS as the target template.
810 Brain surfaces were reconstructed using *recon-all* [FreeSurfer 6.0.1, RRID:SCR_001847, 48], and the brain

811 masks were estimated previously was refined with a custom variation of the method to reconcile ANTs-derived and
812 FreeSurfer-derived segmentations of the cortical gray-matter of Mindboggle [RRID:SCR_002438, 47]. Spatial
813 normalization to the ICBM 152 Nonlinear Asymmetrical template version 2009c [70, RRID:SCR_008796] was
814 performed through nonlinear registration with `antsRegistration` [ANTs 2.2.0, RRID:SCR_004757, 71], using
815 brain-extracted versions of both T1w volume and template. Brain tissue segmentation of cerebrospinal fluid (CSF),
816 white-matter (WM) and gray-matter (GM) was performed on the brain-extracted T1w using `fast` [FSL 5.0.9,
817 RRID:SCR_002823, 72].

818 To preprocess the functional data, a reference volume for each run and its skull-stripped version were generated
819 using a custom methodology of *fMRIPrep*. A deformation field to correct for susceptibility distortions was estimated
820 based on two echo-planar imaging (EPI) references with opposing phase-encoding directions, using `3dQwarp` [73]
821 (AFNI 20160207). Based on the estimated susceptibility distortion, an unwarped BOLD reference was calculated
822 for a more accurate co-registration with the anatomical reference. The BOLD reference was then co-registered
823 to the T1w reference using `bbregister` (FreeSurfer), which implements boundary-based registration [74]. Co-
824 registration was configured with nine degrees of freedom to account for distortions remaining in the BOLD reference.
825 Head-motion parameters with respect to the BOLD reference (transformation matrices, and six corresponding
826 rotation and translation parameters) are estimated before any spatiotemporal filtering using `mcfliirt` [FSL 5.0.9,
827 75]. BOLD runs were slice-time corrected using `3dTshift` from AFNI 20160207 [73, RRID:SCR_005927] and
828 aligned to the middle of each TR. The BOLD time-series (including slice-timing correction) were resampled onto
829 their original, native space by applying a single, composite transform to correct for head-motion and susceptibility
830 distortions. First, a reference volume and its skull-stripped version were generated using a custom methodology of
831 *fMRIPrep*.

832 Several confound regressors were calculated during preprocessing: Six head-motion estimates (see
833 above), Framewise displacement, six anatomical component-based noise correction components (`aCompCor`) and
834 18 physiological parameters (8 respiratory, 6 heart rate and 4 of their interaction). The head-motion estimates
835 were calculated during motion correction (see above). Framewise displacement was calculated for each functional
836 run, using the implementations in *Nipype* [following the definitions by 76]. A set of physiological regressors were
837 extracted to allow for component-based noise correction [*CompCor*, 77]. Principal components are estimated after
838 high-pass filtering the BOLD time-series (using a discrete cosine filter with 128s cut-off) for the two *CompCor*
839 variants: temporal (`tCompCor`, unused) and anatomical (`aCompCor`). For `aCompCor`, six components are calculated
840 within the intersection of the aforementioned mask and the union of CSF and WM masks calculated in T1w space,
841 after their projection to the native space of each functional run (using the inverse BOLD-to-T1w transformation).
842 All resamplings can be performed with a *single interpolation step* by composing all the pertinent transformations
843 (i.e. head-motion transform matrices, susceptibility distortion correction, and co-registrations to anatomical
844 and template spaces). Gridded (volumetric) resamplings were performed using `antsApplyTransforms` (ANTs),
845 configured with Lanczos interpolation to minimize the smoothing effects of other kernels [78]. Lastly, for the
846 18 physiological parameters, correction for physiological noise was performed via RETROICOR [79, 80] using
847 Fourier expansions of different order for the estimated phases of cardiac pulsation (3rd order), respiration (4th
848 order) and cardio-respiratory interactions (1st order) [81]: The corresponding confound regressors were created
849 using the Matlab PhysIO Toolbox ([82], open source code available as part of the TAPAS software collection:
850 <https://www.translationalneuromodeling.org/tapas>. For more details of the pipeline, and details on other
851 confounds generated but not used in our analyses, see the section corresponding to workflows in *fMRIPrep*'s
852 documentation.

853 For univariate analyses, BOLD time-series were re-sampled to MNI152NLin2009cAsym standard space in the
854 *fMRIPrep* pipeline and then smoothed using SPM [83, SPM12 (7771)] with 8mm FWHM, except for ROI
855 generation, where a 4mm FWHM kernel was used. Multivariate analyses were conducted in native space, and data
856 was smoothed with 4mm FWHM using SPM [83, SPM12 (7771)]. Classification analyses further involved three

857 preprocessing steps of voxel time-series: First, extreme-values more than 8 standard deviations from a voxels mean
858 were corrected by moving them by 50% their distance from the mean towards the mean (this was done to not bias
859 the last z scoring step). Second, the time-series of each voxel was detrended, a high-pass filter at 128 Hz was
860 applied and confounds were regressed out in one action using *Nilearn* 0.6.2 [68]. Lastly, the time-series of each
861 voxel for each block was z scored.

862 **Univariate fMRI analysis**

863 All GLMs were conducted using SPM12 [83, SPM12 (7771)] in MATLAB [52]. All GLMs consisted of two regressors
864 of interest corresponding to the onsets of the two trial-types (1D/2D, except for one GLM where 2D onsets were
865 split by Congruency) and included one parametric modulator of EV assigned to 1D onset and different combinations
866 of parametric modulators of EV, Congruency, EV_{back} and their interactions (see Fig. S9 for GLM visualization). All
867 parametric modulators were demeaned before entering the GLM, but not orthogonalized. Regressors of no interest
868 reflected cue onsets in Motion and Color trials, stimulus onsets in wrong and no-answer trials, outcome onsets
869 and 31 nuisance regressors (e.g. motion and physiological parameters, see fMRI-preprocessing). The duration of
870 stimulus regressors corresponded to the time the stimuli were on screen. The durations for the rest of the onset
871 regressors were set to 0. Microtime resolution was set to 16 (64 slices / 4 MB factor) and microtime onset was set to
872 the 8 (since slice time correction aligned to middle slice, see fMRI-preprocessing). Data for all univariate analyses
873 were masked with a whole brain mask computed as intercept of each functional run mask generated from fMRIprep
874 [47, 48]. MNI coordinates were translated to their corresponding brain regions using the automated anatomical
875 parcellation toolbox [84–86, AAL3v1] for SPM. We verified the estimability of the design matrices by assessing
876 the Variance Inflation Factor (VIF) for each onset regressor in the HRF-convolved design matrix. Specifically, for
877 each subject, we computed the VIF (assisted by scripts from <https://github.com/sjgershbm/ccn1-fmri>) for
878 each regressor in the HRF-convolved design matrix and averaged the VIFs of corresponding onsets across the
879 blocks. None of the VIFs surpassed a value of 3.5 (a value of 5 is considered a conservative indicator for overly
880 colinear regressors, e.g. [87], see Fig.S9 for details). Detailed descriptions of all GLMs are reported in the main
881 text. Additional GLMs verifying the lack of Congruency in any frontal region can be found in Fig.S9.

882 **vmPFC functional ROI** In order to generate a functional ROI corresponding to the vmPFC in a reasonable
883 size, we re-ran the GLM with only EV modulators (i.e. this GLM had no information regarding the contextually
884 irrelevant context) on data that was smoothed at 4mm. We then threshold the EV contrasts for 1D and 2D
885 trials ($EV_{1D} + EV_{2D} > 0$) at $p < .0005$. The group ROI was generated in MNI space and included 998 voxels.
886 Multivariate analyses were conducted in native space and the ROI was transformed to native space using ANTs
887 and nearest neighbor interpolation [ANTs 2.2.0 71] while keeping only voxels within the union of subject- and
888 run-specific brain masks produced by the fMRIprep pipeline [47, 48]. The resulting subject-specific ROIs therefore
889 had varying number of voxels ($\mu = 768.14$, $\sigma = 65.62$, $\min = 667$, $\max = 954$).

890 **Multivariate analysis**

891 **Classification procedure** The training set for all analyses consisted of fMRI data from behaviorally accurate 1D
892 trials. For each trial, we took the TR corresponding to approx. 5 seconds after stimulus onset ($\text{round}(\text{onset} + 5)$)
893 to match the peak of the Haemodynamic Response Function (HRF) estimated by SPM [83]. Classification training
894 was done using a leave-one-run-out scheme across the four runs with 1D trials. To avoid bias in the training set
895 after sub-setting only to behaviorally accurate trials (i.e. over-representation of some information) we up-sampled
896 each training set to ensure equal number of examples in the training set for each combination of EV (3), Context
897 (2) and Chosen-Side (2). Specifically, if one particular category was less frequent than another (e.g., more value-30,
898 left, color trials than value-50, left-color trials) we up-sampled that example category by randomly selecting a trial
899 from the same category to duplicate in the training set, whilst prioritising block-wise balance (i.e., if one block

900 had 2 trials in the chunk and another block had only 1, we first duplicated the trial from under-represented block
901 etc.). We did not up-sample the testing set. Decoding was conducted using multinomial logistic regression as
902 implemented in *scikit-learn* 0.22.2 [88] set to multinomial (in opposed to one-vs-all) with C-parameter 1.0, lbgfs
903 solver with a 'l2' penalty for regularization. The classifier provided for each trial in the testing block one probability
904 (or: predicted probability) per class that was given to it. To avoid bias in the modeling of the classifier's predictions
905 (i.e. one probability for each class) we performed outlier-correction, i.e. rounded up values smaller than 0.00001
906 and down values bigger than 0.99999. Due to technical reasons, we averaged the classifier probabilities across the
907 nuisance effects, i.e. obtaining one average probability for each combination of relevant and irrelevant values. This
908 resulted in 36 probabilities per participant, one for each combination of EV level (three levels), irrelevant value of
909 the chosen side and irrelevant value of the non-chosen side (12 combinations, see Fig. 1). Note that the relevant
910 value of the unchosen cloud was always EV - 20 and therefore we did not include this as a parameter of interest.
911 After averaging, we computed for each combination of values the EV_{back} , Congruency and alternative parameters
912 (see Fig. S8). The main model comparison, as well as the lack of effects of any nuisance regressor, was confirmed
913 on a dataset with raw, i.e. non-averaged, probabilities (see Fig S6 and S8). Throughout all the analyses, each
914 regressor was scaled prior to fitting the models. Lastly, for the analysis of $P_{EV_{back}}$ (Fig. 5d.) and for Fig. 7 we
915 also included behaviorally wrong trials.

916 **Verifying design trial-wise estimability** To verify that the individual trials are estimatable and as a control
917 over multi-colinearity [87], we convolved a design matrix with the HRF for each subject with one regressor per
918 stimuli (432 regressors with duration equal to the stimulus duration), two regressor across all cues (split by context)
919 and three regressor for all outcomes (one for each EV). We then computed the VIF for each stimulus regressor (i.e.
920 how predictive is each regressor by the other ones). None of the VIFs surpassed 1.57 across all trials and subjects
921 ($\mu_{VIF} = 1.42, \sigma_{VIF} = .033, \min = 1.34$). When repeating this analysis with a GLM in which also outcomes were
922 split into trialwise regressors, we found no stimuli VIF larger than 3.09 ($\mu_{VIF} = 2.64, \sigma_{VIF} = .132, \min = 1.9$).
923 Note that 1 is the minimum (best) value and 5 is a relatively conservative threshold for colinearity issues ([e.g.
924 87]). This means that the BOLD responses of individual trials can be modeled separately and should not have
925 colinearity issues with other stimuli nor with the outcome presentation of each trial.

926 **Modelling class probabilities** The classifier provided one probability to each class, given the data (all probabilities
927 for each trial sum to 1). Probabilities were analyzed in R (R version 3.6.3 [57], RStudio version 1.3.959 [58])
928 with Generalized Linear Mixed Models using Template Model Builder (glmmTMB, [89]) models, employing a beta
929 distribution family with a 'logit' link function. When describing main effects of models, the χ^2 represents Type II
930 Wald χ^2 tests, whereas when describing model comparison, the χ^2 represents the log-likelihood ratio test. Model
931 comparison throughout the paper was done using the 'anova' function.

932 The value similarity analyses asked whether the predicted probabilities reflected the difference from the objective
933 probability class. The model we found to best explain the data was:

$$P_{t,c}^k = \beta_0 + \gamma_{0k} + \beta_1 |EV_t - Class_{c,t}| + \beta_2 |EV_t - Class_{c,t}| EV_{back_t} \quad (4)$$

934 where $P_{t,c}^k$ is the probability assigned to class c in trial t for subject k , β_0 and γ_{0k} represent global and subject-
935 specific intercepts, $|EV_t - Class_{c,t}|$ is the absolute difference between the EV of the trial and the class the
936 probability is assigned to and $|EV_t - Class_{c,t}| EV_{back_t}$ is the interaction of this absolute difference with EV_{back} .
937 For models nested in the levels of EV, we included $\zeta_{0_{kv}}$, which is the EV-specific intercept nested within each
938 within each subject level.

939 For the feature similarity model we substituted $|EV_t - Class_{c,t}|$ with a "similarity" parameter that encoded the
940 perceptual similarity between each trial in the test set and the perceptual features that constituted the training
941 examples of each class of the classifier. For 1D trials, this perceptual parameter was identical to the value similarity

942 parameter ($|EV_t - Class_{c,t}|$). This was because from the shown pairs of colors, both colors overlapped between
 943 training and test if the values were identical; one color overlapped if the values were different by one reward level
 944 (e.g. a 30 vs 50 comparison corresponded to two trials that involved pink vs green and green vs orange, i.e. sharing
 945 the color green); and no colors overlapped if the values were different by two levels (30 vs 70). On 2D trials
 946 however, due to changing background features and their value-difference variation, perceptual similarity of training
 947 and test was not identical to value similarity. Even though both the value similarity and the perceptual similarity
 948 parameter correlated ($\rho = .789$, $\sigma = .005$), we found that the value similarity model provided a better AIC score
 949 (value similarity AIC: -3898, Feature similarity AIC: -3893, Fig. 4). Detailed description with examples can be
 950 found in Fig. S6. Crucially, even when keeping the value difference of the irrelevant features at 20, thus limiting the
 951 testing set only to trials with feature-pairs that were included in the training, our value similarity model provided a
 952 better AIC (-1959) than the feature similarity model (-1956). To test for a perceptual alternative of EV_{back} we
 953 substituted the corresponding parameter from the model with $Similarity_{back}$. This perceptual parameter takes on
 954 1 if the perceptual feature corresponding to the EV_{back} appeared in the 1D training class (as highest or lowest
 955 value) and 0 otherwise. As described in the main text, none of the perceptual-similarity encoding alternatives
 956 provided a better fit than our models that focused on the expected values the features represented.

957 When modelling the probability of the objective EV, the model we found to explained the data best was:

$$P_{t,EV}^k = \beta_0 + \gamma_{0k} + \beta_1 EV_{back_t} \quad (5)$$

958 where $P_{t,EV}^k$ is the probability assigned to the objective class (corresponding to EV of the trial t) for subject k , β_0
 959 and γ_{0k} represent global and subject-specific intercepts and EV_{back_t} is the maximum of the two ignored values (or
 960 the EV of the contextually irrelevant context). For models nested in the levels of EV, we included $\zeta_{0,k,v}$ which
 961 is EV specific intercept nested within each within each subject level (see Fig. S8). Investigations of alternative
 962 parametrizations of the values can be found in Fig. S8.

963 When modelling the probability of EV_{back} , we did not average across nuisance regressors. Our baseline model was:
 964 $P_{t,EV_{back}}^k = \beta_0 + \gamma_{0k} + \nu_1 side(t) + \nu_2 switch(t) + \nu_3 context(t)$. Neither including a main effect nor interactions
 965 between EV, EV_{back} and Congruency improved model fit. When including behaviorally wrong trials in the model, we
 966 used `drop1` in combination with χ^2 -tests from `lmer4` package [59] to test which of the main effects or interactions
 967 improves the fit. This resulted in the following model as best explaining the data:

$$P_{t,EV_{back}}^k = \beta_0 + \gamma_{0k} + \beta_1 EV_t \times EV_{back_t} + \beta_2 Congruency_t \times Accuracy_t \\ + \nu_1 t + \nu_2 side_t + \nu_3 switch_t + \nu_4 context_t \quad (6)$$

968 where $P_{t,EV_{back}}^k$ is the probability assigned to the EV_{back} class (corresponding to EV_{back} of trial t) for subject k ,
 969 β_0 and γ_{0k} represent global and subject-specific intercepts, EV is the maximum of the two relevant and EV_{back}
 970 is the maximum of the two ignored values. Congruency reflects whether the actions chosen in the relevant vs.
 971 irrelevant context would be the same, and the Accuracy regressor has 1 if participants chose the highest relevant
 972 value and 0 otherwise. We note that the interaction $EV \times EV_{back}$ ($\chi^2_{(1)} = 4.18$, $p = .041$) indicates higher in
 973 trials in which EV and EV_{back} were more similar, the probability assigned to EV_{back} was higher. However, we find
 974 this effect hard to interpret since this corresponds to the value similarity effect we previously reported.

975 **Parallel representation of outcomes in vmPFC.** To compute the correlations between each pair of classes
 976 we transformed the probabilities for each class using a multinomial logit transform. For example, for class 30
 977 we performed probabilities were transformed with $mlogit(P_{t,30}) = 0.5(\log \frac{P_{t,30}}{P_{t,50}} + \log \frac{P_{t,30}}{P_{t,70}})$. To examine the
 978 relationship between EV and EV_{back} , we only included 2D trials in which $EV \neq EV_{back}$. This allowed us to
 979 categorize all three probabilities as either EV, EV_{back} or Other, whereby Other reflected the value that was neither
 980 the EV, nor the EV_{back} . To prevent bias we included only trials in which Other was presented on screen (as relevant

981 or irrelevant value). We then averaged across nuisance regressors (see Classification procedure) and computed
 982 the correlation across all trials. Lastly, we Fisher z-transformed the correlations ($0.5 \log \frac{1+\rho}{1-\rho}$) to approximate
 983 normality for the t test. To validate these results, we performed an additional model comparison in which we
 984 added a term of the logit transformed $P_{EV_{back}}$ or of P_{other} to Eq. 5 ($\beta_2 mlogit(P_{t,EV_{back}})$ or $\beta_2 mlogit(P_{t,Other})$
 985 , respectively). As reported in the main text, adding a term reflecting $P_{EV_{back}}$ resulted in a smaller (better) AIC
 986 score than when we added a term for P_{other} (-567,-475, respectively). This was also preserved when running
 987 the analysis including nuisance regressors (see ν s in Eq. 2) on the non-averaged data (AICs: -5913.3,-5813.3).
 988 We note that subsetting the data the way we did resulted in a strong negative correlation in the design matrix
 989 between EV and EV_{back} ($\rho = -0.798$, averaged across subjects). Although this should not directly influence our
 990 interpretation, we validated the results by using alternative models with effects hierarchically nested within the
 991 levels of EV and EV_{back} (Averaged data AICs: -560, -463, Raw data AICs: -5906.8,-5804.3)

992 **Linking MRI effects to behavior** We showed that subjects who had a stronger effect of Congruency on their
 993 RT also had a stronger effect of EV_{back} on P_{EV} , as well as a stronger correlation between P_{EV} and $P_{EV_{back}}$.
 994 The model used to obtain subject-specific Congruency and Congruency \times EV_{back} slopes was:

$$\begin{aligned} \log RT_t^k = & \beta_0 + \gamma_{0k} + \beta_1 EV + \beta_2 Congruency_t + \beta_3 Congruency_t EV_{back_t} \\ & + \gamma_{1k} Congruency + \gamma_{2k} Congruency + \gamma_{3k} EV_{back_t} \\ & + \nu_1 t + \nu_2 side_t + \nu_3 switch_t + \nu_4 context_t \end{aligned} \quad (7)$$

995 where all the notations are the same as in Eq. 2. γ_{1k} represents the subject-specific slope for Congruency for
 996 subject k and γ_{2k} for the interaction of Congruency and EV_{back} .

997 To extract subject-specific slopes for the effect of EV_{back} on P_{EV} we included a term for this effect ($\gamma_{1k} EV_{back_t}$)
 998 in Eq. 5. Due to model convergence issues, we had to drop the subject-specific intercept (γ_{0k}) in that model.

999 For the correlation of P_{EV} and $P_{EV_{back}}$ we only used trials in which $EV \neq EV_{back}$. Probabilities were first
 1000 multinomial logit and then Fisher z-transformed (see above) and averaged across trials to achieve one correlation
 1001 value per subject. In the main text and in Fig 5 we did not average the data to achieve maximum sensitivity
 1002 to trial-wise variations. The results reported in the main text replicate when running the same procedure while
 1003 averaging the data across nuisance regressors following the multinomial logit transformation ($R = .38$, $p = .023$).

1004 **Context decoding** Classification of task context followed the same procedures as when decoding of EV (see
 1005 'Classification procedure'), albeit the classes given to the classifier for each 1D train example were the context, i.e.
 1006 'Color' or 'Motion'. Up-sampling was done in the same manner, resulting in 4 training sets that are each balanced
 1007 across EV, Context and Side of target object, and balanced block-wise as much as possible.

1008 To perform the analysis shown in Fig. 6d, we included a main effect of $P_{context}$ in Eq. 5 that was logit-transformed
 1009 ($logit(P) = \log \frac{P}{1-P}$) and scaled for each subject, thus adding the term $\beta_2 logit(P_{Context})$. Note that since there
 1010 are only 2 classes, there is no need for multinomial logit transformation.

1011 **Neural representations of EV, EV_{back} and Context as predictors of behavioral accuracy** We used hierarchi-
 1012 cal model comparison to directly test the influence of neural representation of EV, EV_{back} and Context on behavioral
 1013 accuracy separately for congruent and incongruent trials. First, we tested if adding $logit(P_{t,Context})$, $mlogit(P_{t,EV})$
 1014 or $mlogit(P_{t,EV_{back}})$ to Eq. 3, would help to explain the behavioral accuracy better. Because the analysis was
 1015 split for congruent and incongruent trials, we excluded the terms involving a Congruency effect. For incongruent
 1016 trials, only $logit(P_{t,Context})$ improved the fit (LR-tests: $logit(P_{t,Context})$: $\chi^2_{(1)} = 3.66$, $p = .055$, $mlogit(P_{t,EV})$:
 1017 $\chi^2_{(1)} = 0.28$, $p = .599$, $mlogit(P_{t,EV_{back}})$: $\chi^2_{(1)} = 0.0$, $p = .957$). In a second step we then separately tested the
 1018 interactions $logit(P_{t,Context}) \times mlogit(P_{t,EV})$ or $logit(P_{t,Context}) \times mlogit(P_{t,EV_{back}})$ and found that only the

1019 latter had improved the fit ($\chi^2_{(1)} = 1.78, p = .183, \chi^2_{(1)} = 6.33, p = .012$, respectively). For congruent trials,
1020 only $mlogit(P_{t,EV_{back}})$ and marginally $mlogit(P_{t,EV})$ improved the fit (LR-tests: $logit(P_{t,Context})$: $\chi^2_{(1)} = 0.0,$
1021 $p = .922, mlogit(P_{t,EV})$: $\chi^2_{(1)} = 3.5, p = .061, mlogit(P_{t,EV_{back}})$: $\chi^2_{(1)} = 6.48, p = .011$). In a second step we
1022 tested separately the interactions $logit(P_{t,Context}) \times mlogit(P_{t,EV}), logit(P_{t,Context}) \times mlogit(P_{t,EV_{back}})$ or
1023 $mlogit(P_{t,EV_{back}}) \times mlogit(P_{t,EV})$ and found none of these improved model fit when adding them to a model
1024 that included both main effects from the previous step ($\chi^2_{(1)} = 0.34, p = .560, \chi^2_{(1)} = .278, p = .598, \chi^2_{(1)} = 2.49,$
1025 $p = .115$, respectively).

1026 References

- 1027 [1] Daniel Kahneman and Amos Tversky. Prospect theory : An analysis of decisions under risk. *Econometrica*, 47:278,
1028 1979.
- 1029 [2] John O'Doherty, Morten L Kringelbach, Edmund T Rolls, Julia Hornak, and Caroline Andrews. Abstract reward and
1030 punishment representations in the human orbitofrontal cortex. *Nature neuroscience*, 4(1):95–102, 2001.
- 1031 [3] Camillo Padoa-Schioppa and John A Assad. Neurons in the orbitofrontal cortex encode economic value. *Nature*, 441
1032 (7090):223–226, 2006.
- 1033 [4] Oscar Bartra, Joseph T McGuire, and Joseph W Kable. The valuation system: a coordinate-based meta-analysis of bold
1034 fmri experiments examining neural correlates of subjective value. *Neuroimage*, 76:412–427, 2013. ISSN 1053-8119.
- 1035 [5] John A Clithero and Antonio Rangel. Informatic parcellation of the network involved in the computation of subjective
1036 value. *Social cognitive and affective neuroscience*, 9(9):1289–1302, 2014.
- 1037 [6] Hilke Plassmann, John O'doherty, and Antonio Rangel. Orbitofrontal cortex encodes willingness to pay in everyday
1038 economic transactions. *Journal of neuroscience*, 27(37):9984–9988, 2007.
- 1039 [7] Erin L Rich and Jonathan D Wallis. Decoding subjective decisions from orbitofrontal cortex. *Nature neuroscience*, 19
1040 (7):973–980, 2016.
- 1041 [8] Sebastien Ballesta, Weikang Shi, Katherine E Conen, and Camillo Padoa-Schioppa. Values encoded in orbitofrontal
1042 cortex are causally related to economic choices. *Nature*, 2020.
- 1043 [9] Maurizio Corbetta and Gordon L Shulman. Control of goal-directed and stimulus-driven attention in the brain. *Nature
1044 reviews neuroscience*, 3(3):201–215, 2002.
- 1045 [10] Mark G Stokes, Makoto Kusunoki, Natasha Sigala, Hamed Nili, David Gaffan, and John Duncan. Dynamic coding for
1046 cognitive control in prefrontal cortex. *Neuron*, 78(2):364–375, 2013.
- 1047 [11] Yael Niv, Reka Daniel, Andra Geana, Samuel J Gershman, Yuan Chang Leong, Angela Radulescu, and Robert C Wilson.
1048 Reinforcement learning in multidimensional environments relies on attention mechanisms. *Journal of Neuroscience*, 35
1049 (21):8145–8157, 2015. ISSN 0270-6474.
- 1050 [12] Yuan Chang Leong, Angela Radulescu, Reka Daniel, Vivian DeWoskin, and Yael Niv. Dynamic interaction between
1051 reinforcement learning and attention in multidimensional environments. *Neuron*, 93(2):451–463, 2017.
- 1052 [13] Peter H Rudebeck and Elisabeth A Murray. The orbitofrontal oracle: cortical mechanisms for the prediction and
1053 evaluation of specific behavioral outcomes. *Neuron*, 84(6):1143–1156, 2014.
- 1054 [14] Vikram S. Chib, Antonio Rangel, Shinsuke Shimojo, and John P. O'Doherty. Evidence for a common representation
1055 of decision values for dissimilar goods in human ventromedial prefrontal cortex. *Journal of Neuroscience*, 29(39):
1056 12315–12320, 2009. ISSN 0270-6474. doi: 10.1523/JNEUROSCI.2575-09.2009.
- 1057 [15] Daniel McNamee, Antonio Rangel, and John P O'doherty. Category-dependent and category-independent goal-value
1058 codes in human ventromedial prefrontal cortex. *Nature neuroscience*, 16(4):479–485, 2013. ISSN 1097-6266.
- 1059 [16] Gabriel Pelletier and Lesley K Fellows. A critical role for human ventromedial frontal lobe in value comparison of
1060 complex objects based on attribute configuration. *Journal of Neuroscience*, 39(21):4124–4132, 2019.
- 1061 [17] Thorsten Kahnt, Jakob Heinzle, Soyoung Q Park, and John-Dylan Haynes. Decoding different roles for vmPFC and
1062 dlPFC in multi-attribute decision making. *Neuroimage*, 56(2):709–715, 2011.
- 1063 [18] Ulrike Basten, Guido Biele, Hauke R. Heekeren, and Christian J. Fiebach. How the brain integrates costs and
1064 benefits during decision making. *Proceedings of the National Academy of Sciences*, 107(50):21767–21772, 2010. doi:
1065 10.1073/pnas.0908104107.
- 1066 [19] Nitzan Shahar, Rani Moran, Tobias U Hauser, Rogier A Kievit, Daniel McNamee, Michael Moutoussis, Raymond J
1067 Dolan, NSPN Consortium, et al. Credit assignment to state-independent task representations and its relationship with
1068 model-based decision making. *Proceedings of the National Academy of Sciences*, 116(32):15871–15876, 2019.
- 1069 [20] Vickie Li, Elizabeth Michael, Jan Balaguer, Santiago Herce Castañón, and Christopher Summerfield. Gain control
1070 explains the effect of distraction in human perceptual, cognitive, and economic decision making. *Proceedings of the
1071 National Academy of Sciences*, 115(38):E8825–E8834, 2018. ISSN 0027-8424.
- 1072 [21] Valerio Mante, David Sussillo, Krishna V Shenoy, and William T Newsome. Context-dependent computation by
1073 recurrent dynamics in prefrontal cortex. *nature*, 503(7474):78, 2013. ISSN 1476-4687.
- 1074 [22] Yu Takagi, Laurence T Hunt, Mark W Woolrich, Timothy EJ Behrens, and Miriam Klein-Flugge. Projections of
1075 non-invasive human recordings into state space show unfolding of spontaneous and over-trained choice. *bioRxiv*, 2020.
- 1076 [23] Nicolas W Schuck, Robert Gaschler, Dorit Wenke, Jakob Heinzle, Peter A Frensch, John-Dylan Haynes, and Carlo
1077 Reverberi. Medial prefrontal cortex predicts internally driven strategy shifts. *Neuron*, 86(1):331–340, 2015.
- 1078 [24] Brian A Anderson. A value-driven mechanism of attentional selection. *Journal of vision*, 13(3):7–7, 2013.
- 1079 [25] Marcus Grueschow, Rafael Polania, Todd A Hare, and Christian C Ruff. Automatic versus choice-dependent value
1080 representations in the human brain. *Neuron*, 85(4):874–885, 2015.

- 1081 [26] Maël Lebreton, Soledad Jorge, Vincent Michel, Bertrand Thirion, and Mathias Pessiglione. An automatic valuation
1082 system in the human brain: Evidence from functional neuroimaging. *Neuron*, 64(3):431 – 439, 2009. ISSN 0896-6273.
1083 doi: <https://doi.org/10.1016/j.neuron.2009.09.040>.
- 1084 [27] Margaret L Schlichting, Jeanette A Mumford, and Alison R Preston. Learning-related representational changes reveal
1085 dissociable integration and separation signatures in the hippocampus and prefrontal cortex. *Nature communications*, 6
1086 (1):1–10, 2015.
- 1087 [28] Geoffrey Schoenbaum and Matthew Roesch. Orbitofrontal cortex, associative learning, and expectancies. *Neuron*, 47
1088 (5):633–636, 2005.
- 1089 [29] Michael L Mack, Alison R Preston, and Bradley C Love. Ventromedial prefrontal cortex compression during concept
1090 learning. *Nature communications*, 11(1):1–11, 2020.
- 1091 [30] Christian F Doeller, Caswell Barry, and Neil Burgess. Evidence for grid cells in a human memory network. *Nature*, 463
1092 (7281):657–661, 2010.
- 1093 [31] Alexandra O Constantinescu, Jill X O’Reilly, and Timothy EJ Behrens. Organizing conceptual knowledge in humans
1094 with a gridlike code. *Science*, 352(6292):1464–1468, 2016.
- 1095 [32] Nicolas W Schuck, Ming Bo Cai, Robert C Wilson, and Yael Niv. Human orbitofrontal cortex represents a cognitive
1096 map of state space. *Neuron*, 91(6):1402–1412, 2016.
- 1097 [33] Stephanie CY Chan, Yael Niv, and Kenneth A Norman. A probability distribution over latent causes, in the orbitofrontal
1098 cortex. *Journal of Neuroscience*, 36(30):7817–7828, 2016.
- 1099 [34] Nicolas W Schuck, Robert Wilson, and Yael Niv. A state representation for reinforcement learning and decision-making
1100 in the orbitofrontal cortex. In *Goal-directed decision making*, pages 259–278. Elsevier, 2018.
- 1101 [35] G Elliott Wimmer and Christian Büchel. Learning of distant state predictions by the orbitofrontal cortex in humans.
1102 *Nature communications*, 10(1):1–11, 2019.
- 1103 [36] Jingfeng Zhou, Matthew PH Gardner, Thomas A Stalnaker, Seth J Ramus, Andrew M Wikenheiser, Yael Niv, and
1104 Geoffrey Schoenbaum. Rat orbitofrontal ensemble activity contains multiplexed but dissociable representations of value
1105 and task structure in an odor sequence task. *Current Biology*, 29(6):897–907, 2019.
- 1106 [37] Anja Farovik, Ryan J Place, Sam McKenzie, Blake Porter, Catherine E Munro, and Howard Eichenbaum. Orbitofrontal
1107 cortex encodes memories within value-based schemas and represents contexts that guide memory retrieval. *Journal of*
1108 *Neuroscience*, 35(21):8333–8344, 2015.
- 1109 [38] Praveen K Pilly and Aaron R Seitz. What a difference a parameter makes: A psychophysical comparison of random
1110 dot motion algorithms. *Vision research*, 49(13):1599–1612, 2009. ISSN 0042-6989.
- 1111 [39] Denis Cousineau et al. Confidence intervals in within-subject designs: A simpler solution to Loftus and Masson’s
1112 method. *Tutorials in quantitative methods for psychology*, 1(1):42–45, 2005.
- 1113 [40] Richard D Morey et al. Confidence intervals from normalized data: A correction to Cousineau (2005). *reason*, 4(2):
1114 61–64, 2008.
- 1115 [41] Laurence T Hunt, Nils Kolling, Alireza Soltani, Mark W Woolrich, Matthew FS Rushworth, and Timothy EJ Behrens.
1116 Mechanisms underlying cortical activity during value-guided choice. *Nature neuroscience*, 15(3):470–476, 2012. ISSN
1117 1097-6256.
- 1118 [42] Satoshi Tajima, Jan Drugowitsch, and Alexandre Pouget. Optimal policy for value-based
1119 decision-making. *Nature Communications*, 7:12400, 2016. doi: 10.1038/ncomms12400
1120 <https://www.nature.com/articles/ncomms12400supplementary-information>. URL <https://doi.org/10.1038/ncomms12400>.
- 1121
- 1122 [43] Ian Krajbich, Björn Bartling, Todd Hare, and Ernst Fehr. Rethinking fast and slow based on a critique of reaction-time
1123 reverse inference. *Nature Communications*, 6:7455, 2015. doi: 10.1038/ncomms8455. URL <https://doi.org/10.1038/ncomms8455>.
- 1124
- 1125 [44] Arni Magnusson, Hans Skaug, Anders Nielsen, Casper Berg, Kasper Kristensen, Martin Maechler, Koen van Benthem,
1126 Ben Bolker, Mollie Brooks, and Maintainer Mollie Brooks. Package ‘glmmTMB’. *R Package Version 0.2.0*, 2017.
- 1127 [45] Robert C Wilson, Yuji K Takahashi, Geoffrey Schoenbaum, and Yael Niv. Orbitofrontal cortex as a cognitive map of
1128 task space. *Neuron*, 81(2):267–279, 2014.
- 1129 [46] Yael Niv. Learning task-state representations. *Nature neuroscience*, 22(10):1544–1553, 2019.
- 1130 [47] Arno Klein, Satrajit S. Ghosh, Forrest S. Bao, Joachim Giard, Yrjö Häme, Eliezer Stavsky, Noah Lee, Brian Rossa,
1131 Martin Reuter, Elias Chaibub Neto, and Anisha Keshavan. Mindboggling morphometry of human brains. *PLoS*
1132 *Computational Biology*, 13(2):e1005350, 2017. ISSN 1553-7358. doi: 10.1371/journal.pcbi.1005350. URL <http://journals.plos.org/ploscompbiol/article?id=10.1371/journal.pcbi.1005350>.
- 1133
- 1134 [48] Anders M. Dale, Bruce Fischl, and Martin I. Sereno. Cortical surface-based analysis: I. segmentation and surface
1135 reconstruction. *NeuroImage*, 9(2):179–194, 1999. ISSN 1053-8119. doi: 10.1006/nimg.1998.0395. URL <http://www.sciencedirect.com/science/article/pii/S1053811998903950>.
- 1136

- 1137 [49] David H Brainard and Spatial Vision. The psychophysics toolbox. *Spatial vision*, 10:433–436, 1997.
- 1138 [50] Denis G Pelli and Spatial Vision. The videotoolbox software for visual psychophysics: Transforming numbers into
1139 movies. *Spatial vision*, 10:437–442, 1997.
- 1140 [51] Mario Kleiner, David Brainard, Denis Pelli, Allen Ingling, Richard Murray, Christopher Broussard, et al. What's new in
1141 psychtoolbox-3. *Perception*, 36(14):1, 2007.
- 1142 [52] *MATLAB version 9.3.0.713579 (R2017b)*. The Mathworks, Inc., Natick, Massachusetts, 2017.
- 1143 [53] *MATLAB version (R2012b)*. The Mathworks, Inc., Natick, Massachusetts, 2017.
- 1144 [54] Joshua T Abbott, Thomas L Griffiths, and Terry Regier. Focal colors across languages are representative members of
1145 color categories. *Proceedings of the National Academy of Sciences*, 113(40):11178–11183, 2016. ISSN 0027-8424.
- 1146 [55] Helen C Barron, Mona M Garvert, and Timothy EJ Behrens. Repetition suppression: a means to index neural
1147 representations using bold? *Philosophical Transactions of the Royal Society B: Biological Sciences*, 371(1705):
1148 20150355, 2016.
- 1149 [56] Mona M Garvert, Raymond J Dolan, and Timothy EJ Behrens. A map of abstract relational knowledge in the human
1150 hippocampal–entorhinal cortex. *Elife*, 6:e17086, 2017.
- 1151 [57] R Core Team. *R: A Language and Environment for Statistical Computing*. R Foundation for Statistical Computing,
1152 Vienna, Austria, 2017. URL <https://www.R-project.org/>.
- 1153 [58] RStudio Team. *RStudio: Integrated Development Environment for R*. RStudio, PBC., Boston, MA, 2020. URL
1154 <http://www.rstudio.com/>.
- 1155 [59] Douglas Bates, Martin Mächler, Ben Bolker, and Steve Walker. Fitting linear mixed-effects models using lme4. *Journal*
1156 *of Statistical Software*, 67(1):1–48, 2015. doi: 10.18637/jss.v067.i01.
- 1157 [60] Nikolaus Weiskopf, Chloe Hutton, Oliver Josephs, and Ralf Deichmann. Optimal epi parameters for reduction of
1158 susceptibility-induced bold sensitivity losses: A whole-brain analysis at 3 t and 1.5 t. *NeuroImage*, 33(2):493 – 504,
1159 2006. ISSN 1053-8119. doi: <https://doi.org/10.1016/j.neuroimage.2006.07.029>.
- 1160 [61] Krzysztof J Gorgolewski, Tibor Auer, Vince D Calhoun, R Cameron Craddock, Samir Das, Eugene P Duff, Guillaume
1161 Flandin, Satrajit S Ghosh, Tristan Glatard, Yaroslav O Halchenko, et al. The brain imaging data structure, a format
1162 for organizing and describing outputs of neuroimaging experiments. *Scientific data*, 3(1):1–9, 2016.
- 1163 [62] Xiangrui Li, Paul S Morgan, John Ashburner, Jolinda Smith, and Christopher Rorden. The first step for neuroimaging
1164 data analysis: Dicom to nifti conversion. *Journal of neuroscience methods*, 264:47–56, 2016.
- 1165 [63] Oscar Esteban, Daniel Birman, Marie Schaer, Oluwasanmi O Koyejo, Russell A Poldrack, and Krzysztof J Gorgolewski.
1166 Mriqc: Advancing the automatic prediction of image quality in mri from unseen sites. *PLoS one*, 12(9):e0184661, 2017.
- 1167 [64] Oscar Esteban, Christopher Markiewicz, Ross W Blair, Craig Moodie, Ayse Ilkay Isik, Asier Erramuzpe Aliaga, James
1168 Kent, Mathias Goncalves, Elizabeth DuPre, Madeleine Snyder, Hiroyuki Oya, Satrajit Ghosh, Jessey Wright, Joke
1169 Durnez, Russell Poldrack, and Krzysztof Jacek Gorgolewski. fMRIPrep: a robust preprocessing pipeline for functional
1170 MRI. *Nature Methods*, 2018. doi: 10.1038/s41592-018-0235-4.
- 1171 [65] Oscar Esteban, Ross Blair, Christopher J. Markiewicz, Shoshana L. Berleant, Craig Moodie, Feilong Ma, Ayse Ilkay
1172 Isik, Asier Erramuzpe, Mathias Kent, James D. and Goncalves, Elizabeth DuPre, Kevin R. Sitek, Daniel E. P. Gomez,
1173 Daniel J. Lurie, Zhifang Ye, Russell A. Poldrack, and Krzysztof J. Gorgolewski. fmriprep. *Software*, 2018. doi:
1174 10.5281/zenodo.852659.
- 1175 [66] K. Gorgolewski, C. D. Burns, C. Madison, D. Clark, Y. O. Halchenko, M. L. Waskom, and S. Ghosh. Nipype: a flexible,
1176 lightweight and extensible neuroimaging data processing framework in python. *Frontiers in Neuroinformatics*, 5:13,
1177 2011. doi: 10.3389/fninf.2011.00013.
- 1178 [67] Krzysztof J. Gorgolewski, Oscar Esteban, Christopher J. Markiewicz, Erik Ziegler, David Gage Ellis, Michael Philipp
1179 Notter, Dorota Jarecka, Hans Johnson, Christopher Burns, Alexandre Manhães-Savio, Carlo Hamalainen, Benjamin
1180 Yvernault, Taylor Salo, Keshi Jordan, Mathias Goncalves, Michael Waskom, Daniel Clark, Jason Wong, Fred Loney,
1181 Marc Modat, Blake E Dewey, Cindee Madison, Matteo Visconti di Oleggio Castello, Michael G. Clark, Michael Dayan,
1182 Dav Clark, Anisha Keshavan, Basile Pinsard, Alexandre Gramfort, Shoshana Berleant, Dylan M. Nielson, Salma
1183 Bougacha, Gael Varoquaux, Ben Cipollini, Ross Markello, Ariel Rokem, Brendan Moloney, Yaroslav O. Halchenko,
1184 Demian Wassermann, Michael Hanke, Christian Horea, Jakub Kaczmarzyk, Gilles de Hollander, Elizabeth DuPre,
1185 Ashley Gillman, David Mordom, Colin Buchanan, Rosalia Tungaraza, Wolfgang M. Pauli, Shariq Iqbal, Sharad
1186 Sikka, Matteo Mancini, Yannick Schwartz, Ian B. Malone, Mathieu Dubois, Caroline Frohlich, David Welch, Jessica
1187 Forbes, James Kent, Aimi Watanabe, Chad Cumba, Julia M. Huntenburg, Erik Kastman, B. Nolan Nichols, Arman
1188 Eshaghi, Daniel Ginsburg, Alexander Schaefer, Benjamin Acland, Steven Giavasis, Jens Kleesiek, Drew Erickson, René
1189 Küttner, Christian Haselgrove, Carlos Correa, Ali Ghayoor, Franz Liem, Jarrod Millman, Daniel Haehn, Jeff Lai, Dale
1190 Zhou, Ross Blair, Tristan Glatard, Mandy Renfro, Siqi Liu, Ari E. Kahn, Fernando Pérez-García, William Triplett,
1191 Leonie Lampe, Jörg Stadler, Xiang-Zhen Kong, Michael Hallquist, Andrey Chetverikov, John Salvatore, Anne Park,
1192 Russell Poldrack, R. Cameron Craddock, Souheil Inati, Oliver Hinds, Gavin Cooper, L. Nathan Perkins, Ana Marina,
1193 Aaron Mattfeld, Maxime Noel, Lukas Snoek, K Matsubara, Brian Cheung, Simon Rothmei, Sebastian Urchs, Joke
1194 Durnez, Fred Mertz, Daniel Geisler, Andrew Floren, Stephan Gerhard, Paul Sharp, Miguel Molina-Romero, Alejandro

- 1195 Weinstein, William Broderick, Victor Saase, Sami Kristian Andberg, Robbert Harms, Kai Schlamp, Jaime Arias, Dimitri
1196 Papadopoulos Orfanos, Claire Tarbert, Arielle Tambini, Alejandro De La Vega, Thomas Nickson, Matthew Brett, Marcel
1197 Falkiewicz, Kornelius Podranski, Janosch Linkersdörfer, Guillaume Flandin, Eduard Ort, Dmitry Shachnev, Daniel
1198 McNamee, Andrew Davison, Jan Varada, Isaac Schwabacher, John Pellman, Martin Perez-Guevara, Ranjeet Khanuja,
1199 Nicolas Pannetier, Conor McDermottroe, and Satrajit Ghosh. Nipype. *Software*, 2018. doi: 10.5281/zenodo.596855.
- 1200 [68] Alexandre Abraham, Fabian Pedregosa, Michael Eickenberg, Philippe Gervais, Andreas Mueller, Jean Kossaifi, Alexandre
1201 Gramfort, Bertrand Thirion, and Gael Varoquaux. Machine learning for neuroimaging with scikit-learn. *Frontiers in*
1202 *Neuroinformatics*, 8, 2014. ISSN 1662-5196. doi: 10.3389/fninf.2014.00014. URL [https://www.frontiersin.org/](https://www.frontiersin.org/articles/10.3389/fninf.2014.00014/full)
1203 [articles/10.3389/fninf.2014.00014/full](https://www.frontiersin.org/articles/10.3389/fninf.2014.00014/full).
- 1204 [69] N. J. Tustison, B. B. Avants, P. A. Cook, Y. Zheng, A. Egan, P. A. Yushkevich, and J. C. Gee. N4itk: Im-
1205 proved n3 bias correction. *IEEE Transactions on Medical Imaging*, 29(6):1310–1320, 2010. ISSN 0278-0062. doi:
1206 10.1109/TMI.2010.2046908.
- 1207 [70] VS Fonov, AC Evans, RC McKinstry, CR Almlí, and DL Collins. Unbiased nonlinear average age-appropriate brain
1208 templates from birth to adulthood. *NeuroImage*, 47, Supplement 1:S102, 2009. ISSN 1053-8119. doi: 10.1016/S1053-
1209 8119(09)70884-5. URL <http://www.sciencedirect.com/science/article/pii/S1053811909708845>.
- 1210 [71] B.B. Avants, C.L. Epstein, M. Grossman, and J.C. Gee. Symmetric diffeomorphic image registration with cross-
1211 correlation: Evaluating automated labeling of elderly and neurodegenerative brain. *Medical Image Analysis*, 12(1):
1212 26–41, 2008. ISSN 1361-8415. doi: 10.1016/j.media.2007.06.004. URL [http://www.sciencedirect.com/science/](http://www.sciencedirect.com/science/article/pii/S1361841507000606)
1213 [article/pii/S1361841507000606](http://www.sciencedirect.com/science/article/pii/S1361841507000606).
- 1214 [72] Y. Zhang, M. Brady, and S. Smith. Segmentation of brain MR images through a hidden markov random field model and
1215 the expectation-maximization algorithm. *IEEE Transactions on Medical Imaging*, 20(1):45–57, 2001. ISSN 0278-0062.
1216 doi: 10.1109/42.906424.
- 1217 [73] Robert W. Cox and James S. Hyde. Software tools for analysis and visualization of fmri data. *NMR in Biomedicine*,
1218 10(4-5):171–178, 1997. doi: 10.1002/(SICI)1099-1492(199706/08)10:4/5<171::AID-NBM453>3.0.CO;2-L.
- 1219 [74] Douglas N Greve and Bruce Fischl. Accurate and robust brain image alignment using boundary-based registration.
1220 *NeuroImage*, 48(1):63–72, 2009. ISSN 1095-9572. doi: 10.1016/j.neuroimage.2009.06.060.
- 1221 [75] Mark Jenkinson, Peter Bannister, Michael Brady, and Stephen Smith. Improved optimization for the robust and accurate
1222 linear registration and motion correction of brain images. *NeuroImage*, 17(2):825–841, 2002. ISSN 1053-8119. doi:
1223 10.1006/nimg.2002.1132. URL <http://www.sciencedirect.com/science/article/pii/S1053811902911328>.
- 1224 [76] Jonathan D. Power, Anish Mitra, Timothy O. Laumann, Abraham Z. Snyder, Bradley L. Schlaggar, and Steven E.
1225 Petersen. Methods to detect, characterize, and remove motion artifact in resting state fmri. *NeuroImage*, 84(Supplement
1226 C):320–341, 2014. ISSN 1053-8119. doi: 10.1016/j.neuroimage.2013.08.048. URL [http://www.sciencedirect.](http://www.sciencedirect.com/science/article/pii/S1053811913009117)
1227 [com/science/article/pii/S1053811913009117](http://www.sciencedirect.com/science/article/pii/S1053811913009117).
- 1228 [77] Yashar Behzadi, Khaled Restom, Joy Liau, and Thomas T. Liu. A component based noise correction
1229 method (CompCor) for BOLD and perfusion based fmri. *NeuroImage*, 37(1):90–101, 2007. ISSN 1053-
1230 8119. doi: 10.1016/j.neuroimage.2007.04.042. URL [http://www.sciencedirect.com/science/article/pii/](http://www.sciencedirect.com/science/article/pii/S1053811907003837)
1231 [S1053811907003837](http://www.sciencedirect.com/science/article/pii/S1053811907003837).
- 1232 [78] C. Lanczos. Evaluation of noisy data. *Journal of the Society for Industrial and Applied Mathematics Series B Numerical*
1233 *Analysis*, 1(1):76–85, 1964. ISSN 0887-459X. doi: 10.1137/0701007. URL [http://epubs.siam.org/doi/10.1137/](http://epubs.siam.org/doi/10.1137/0701007)
1234 [0701007](http://epubs.siam.org/doi/10.1137/0701007).
- 1235 [79] Gary H Glover, Tie-Qiang Li, and David Ress. Image-based method for retrospective correction of physiological motion
1236 effects in fmri: Retroicor. *Magnetic Resonance in Medicine: An Official Journal of the International Society for*
1237 *Magnetic Resonance in Medicine*, 44(1):162–167, 2000.
- 1238 [80] Chloe Hutton, Oliver Josephs, Jörg Stadler, Eric Featherstone, Alphonso Reid, Oliver Speck, Johannes Bernarding, and
1239 Nikolaus Weiskopf. The impact of physiological noise correction on fmri at 7 t. *NeuroImage*, 57(1):101–112, 2011.
- 1240 [81] Ann K Harvey, Kyle TS Pattinson, Jonathan CW Brooks, Stephen D Mayhew, Mark Jenkinson, and Richard G Wise.
1241 Brainstem functional magnetic resonance imaging: disentangling signal from physiological noise. *Journal of Magnetic*
1242 *Resonance Imaging: An Official Journal of the International Society for Magnetic Resonance in Medicine*, 28(6):
1243 1337–1344, 2008.
- 1244 [82] Lars Kasper, Steffen Bollmann, Andreea O Diaconescu, Chloe Hutton, Jakob Heinze, Sandra Iglesias, Tobias U Hauser,
1245 Miriam Sebold, Zina-Mary Manjaly, Klaas P Pruessmann, et al. The physio toolbox for modeling physiological noise in
1246 fmri data. *Journal of neuroscience methods*, 276:56–72, 2017.
- 1247 [83] William D Penny, Karl J Friston, John T Ashburner, Stefan J Kiebel, and Thomas E Nichols. *Statistical parametric*
1248 *mapping: the analysis of functional brain images*. Elsevier, 2011.
- 1249 [84] Nathalie Tzourio-Mazoyer, Brigitte Landeau, Dimitri Papathanassiou, Fabrice Crivello, Olivier Etard, Nicolas Delcroix,
1250 Bernard Mazoyer, and Marc Joliot. Automated anatomical labeling of activations in spm using a macroscopic anatomical
1251 parcellation of the mni mri single-subject brain. *NeuroImage*, 15(1):273–289, 2002.

- 1252 [85] Edmund T Rolls, Marc Joliot, and Nathalie Tzourio-Mazoyer. Implementation of a new parcellation of the orbitofrontal
1253 cortex in the automated anatomical labeling atlas. *Neuroimage*, 122:1–5, 2015.
- 1254 [86] Edmund T Rolls, Chu-Chung Huang, Ching-Po Lin, Jianfeng Feng, and Marc Joliot. Automated anatomical labelling
1255 atlas 3. *NeuroImage*, 206:116189, 2020.
- 1256 [87] Jeanette A Mumford, Jean-Baptiste Poline, and Russell A Poldrack. Orthogonalization of regressors in fmri models.
1257 *PloS one*, 10(4):e0126255, 2015.
- 1258 [88] F. Pedregosa, G. Varoquaux, A. Gramfort, V. Michel, B. Thirion, O. Grisel, M. Blondel, P. Prettenhofer, R. Weiss,
1259 V. Dubourg, J. Vanderplas, A. Passos, D. Cournapeau, M. Brucher, M. Perrot, and E. Duchesnay. Scikit-learn:
1260 Machine learning in Python. *Journal of Machine Learning Research*, 12:2825–2830, 2011.
- 1261 [89] Mollie E. Brooks, Kasper Kristensen, Koen J. van Benthem, Arni Magnusson, Casper W. Berg, Anders Nielsen,
1262 Hans J. Skaug, Martin Maechler, and Benjamin M. Bolker. glmmTMB balances speed and flexibility among
1263 packages for zero-inflated generalized linear mixed modeling. *The R Journal*, 9(2):378–400, 2017. URL <https://journal.r-project.org/archive/2017/RJ-2017-066/index.html>.
1264

1265 **Supplementary Information**

- 1266 • Fig. S1: Full procedure and experimental design for all phases, related to Fig 1
- 1267 • Fig. S2: Nested RT models, related to Fig 2
- 1268 • Fig. S3: Alternative RT models, extended RT model comparisons and correlation matrix of all regressors,
1269 related to Fig 2
- 1270 • Fig. S4: Exploratory analysis of RT model presented in Main Text, related to Fig 2
- 1271 • Fig. S5: Behavioral accuracy results: related to Fig 2
- 1272 • Fig. S6: Supplementary information for Value similarity analysis: related to Fig. 4
- 1273 • Fig. S7: Supplementary information for perceptual similarity analysis: related to Fig. 4
- 1274 • Fig. S8: Modelling probability assigned to the EV class: related to Fig. 5
- 1275 • Fig. S9: Additional univariate results, related to Fig. 8
- 1276 • Table S1: Detailed univariate results: Clusters for whole brain univariate analysis, related to Fig. 8

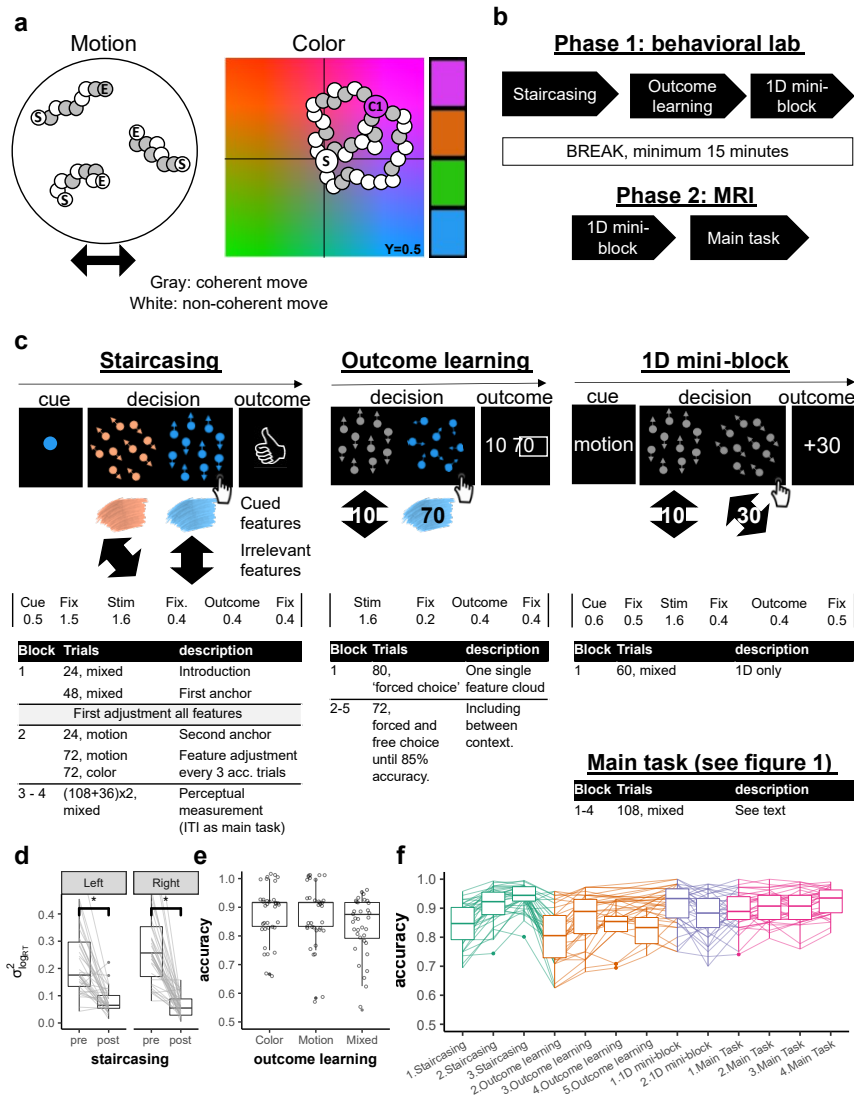


Figure S1: Full procedure and experimental design for all phases

1277 **Figure S1: Full procedure and experimental design for all phases, related to Fig 1.** **a.** Brownian algorithm
 1278 for color and motion. Each illustration shows the course of 3 example dots; 'S' and 'E' marked dots reflect Start
 1279 and End positions, respectively. Remaining dots represent location in space for different frames. Left panel:
 1280 Horizontal motion trial. Shown are framewise dot positions between start and end. In each frame, a different set
 1281 of dots moved coherently in the designated direction (gray) with a fixed speed; remaining dots moved in a random
 1282 direction [conceptually taken from 38]. Right panel: Example of a pink color trial. We simulated the YCbCr color
 1283 space that is believed to represent the human perception in a relative accurate way [cf. 54]. A fixed luminance of
 1284 $Y = 0.5$ was used. For technical reasons we sliced the X-axis by 0.1 on each side and the Y-axis by 0.2 from the
 1285 bottom of the space to ensure the middle of the space remained gray given the chosen luminance. In each frame,
 1286 a different set of dots (always 30% of the dots) moved coherently towards the target color in a certain speed
 1287 whereas the rest were assigned with a random direction. All target colors were offset by 23.75% from the center
 1288 towards each corner. Right bar illustrates the used target colors. **b.** Full procedure. The experiment consisted of
 1289 two phases, the first one took place in the behavioral lab and included Staircasing, Outcome-learning and the first
 1290 1D mini-block. The second took place inside the MRI scanner and consisted of the second 1D mini-block and the
 1291 main task. **c.** Example trial procedures and timing of the different tasks. Timing of each trial is depicted below

1292 illustrations. **Staircasing (left)** Each trial started with a cue of the relevant feature. Each cloud had one or two
1293 features (motion and/or color) and participants had to detect the cued feature. Participants' task was to choose
1294 the cued feature (here: blue). After a choice, participants received feedback if they were correct and faster than
1295 1 second, correct and slower, or wrong. **Outcome learning (middle)** Participants were presented with either
1296 one or two single-feature clouds and asked to choose the highest valued feature. Following their choice, they were
1297 presented with the values of both clouds, with the chosen cloud's associated value marked with a square around
1298 it. The pair of shown stimuli included across contexts comparisons, e.g. between up/right and blue, as shown.
1299 **1D mini block (right)** At the end of the first phase and beginning of the second phase participants completed a
1300 mini-block of 60 1D trials during the anatomical scan (30 color-only, 30 motion-only, interleaved). Participants
1301 were again asked to make a value-based two alternative forced choice decision. In each trial, they were
1302 first presented with a contextual cue (color/motion), followed by the presentation of two single-feature clouds of
1303 the cued context. After a choice, they were presented with the chosen-cloud's value. No BOLD response was
1304 measured during these blocks and timing of the trials was fixed and shorter than in the main task (see Main task
1305 preparation in online methods) **Main task (bottom)** This part included 4 blocks, each consisting of 36 1D and
1306 72 2D trials presented in an interleaved fashion (see online method and Fig. 1). **d.** Button specific reduction
1307 in RT variance following the staircasing. We verified that the staircasing procedure also reduced differences
1308 in detection speed between features when testing each button separately. Depicted is the variance of reaction
1309 times (RTs) across different color and motion features (y axis). While participants' RTs were markedly different
1310 for different features before staircasing (pre), a significant reduction in RT differences was observed after the
1311 procedure (post, $p < .001$.) **e.** Choice accuracy in outcome learning trials. Participants achieved near ceiling
1312 accuracy in choosing the highest valued feature in the outcome learning task, also when testing for color, motion
1313 and mixed trials separately ($ps < .001$). Mixed trials only appeared in this part of the experiment to encourage
1314 mapping of the values on similar scales. **f.** Accuracy throughout the experiment, plotted for each block of each
1315 part of the experiment. *In the staircasing (left)* High accuracy for the adjustment and measurement blocks (2-3)
1316 ensured that there were no difficulties in perceptual detection of the features. *In Outcome learning* a clear increase
1317 in accuracy throughout this task indicated learning of feature-outcome associations. Note that Block 5 of this
1318 part was only included for those who did not achieve 85% accuracy beforehand. Starting the *1D mini blocks*
1319 (middle) and throughout the *main task* (right) until the end of the experiment high accuracy. μ and σ from left
1320 to right: Staircasing: .84,.07;.91,.06;.94,.04; Outcome Learning: .81,.1;.86,.09;.83,.08;.82,.06; 1D mini blocks:
1321 .91,.07;.88,.08; Main task: .89,.06;.91,.05;.9,.06;.92,.05.

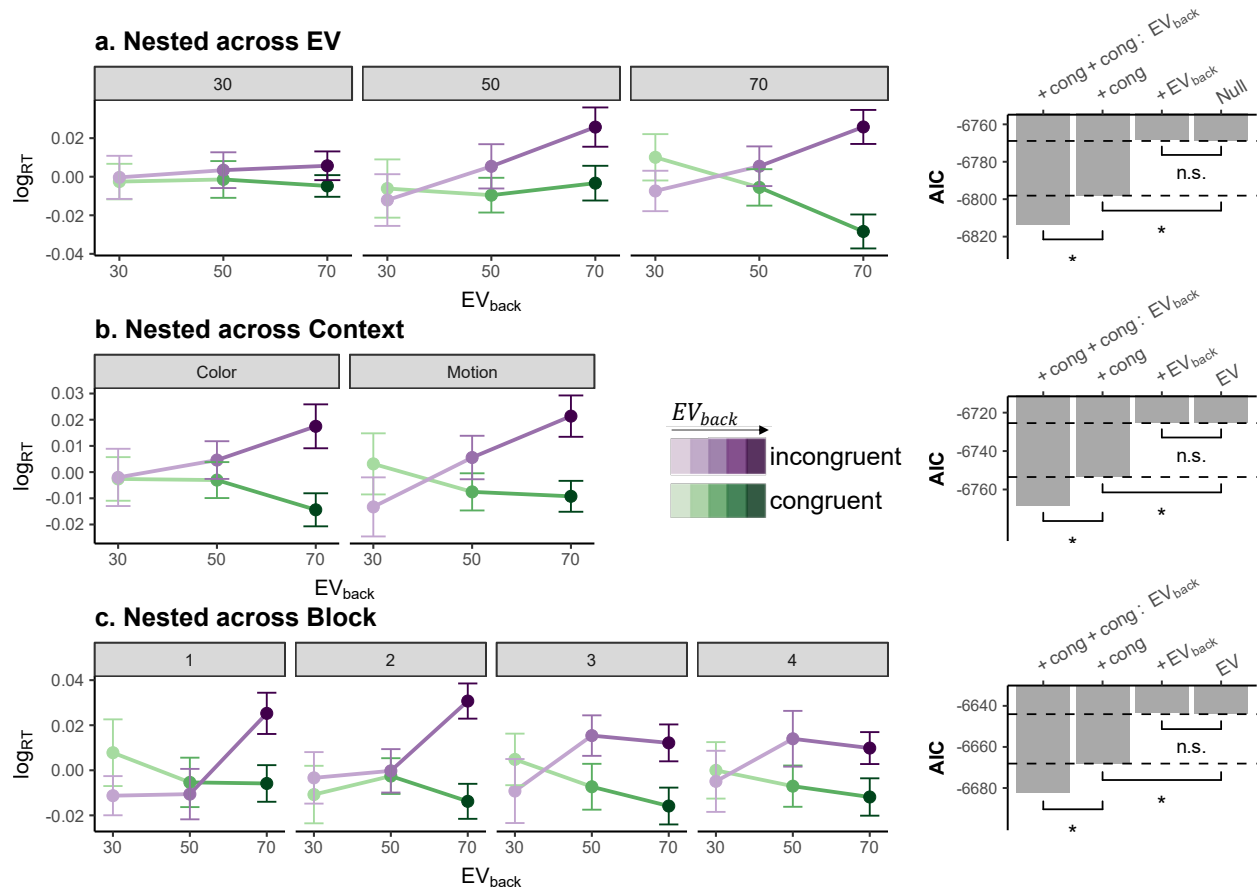


Figure S2: Nested RT models, related to Fig 2

1322 **Figure S2: Nested RT models, related to Fig 2**

1323 **a-c. Nested models within Factors.** Each row represents one congruency analysis, done separately for each
 1324 level of expected value (top row), context (middle) or block (bottom). The RT effect of $\text{Congruency}_t \times \text{EV}_{\text{back}t}$
 1325 is shown on the left, corresponding AICs for mixed effect models with nested factors are shown on the right. RT data
 1326 is demeaned for each panel for visual comparison; error bars represent corrected within subject SEMs [39, 40]. Null
 1327 models shown on the right are identical to Eq. 2, albeit included $\zeta_{0_{kv}}$, which is the factor-specific (v) intercept
 1328 nested within each within each subject level (see online methods). Likelihood ratio tests were performed to assess
 1329 improved model fit when adding (1) Congruency or (2) EV_{back} terms to the Null model and when adding (3)
 1330 $\text{Congruency} \times \text{EV}_{\text{back}}$ in addition to Congruency. Stars represent p values less than .05. For nested within EV, the
 1331 Null model did not include a main effect for EV and the LR test was: (1) $\chi^2_{(1)} = 31.22, p < .001$; (2) $\chi^2_{(1)} = 1.47,$
 1332 $p = .226$; (3) $\chi^2_{(1)} = 19.37, p < .001$; For models nested within Context the LR test was: (1) $\chi^2_{(1)} = 30.01,$
 1333 $p < .001$; (2) $\chi^2_{(1)} = 1.5, p = .22$; (3) $\chi^2_{(1)} = 18.9, p < .001$; and for Block: (1) $\chi^2_{(1)} = 26.06, p < .001$; (2)
 1334 $\chi^2_{(1)} = 1.27, p = .26$; (3) $\chi^2_{(1)} = 18.25, p < .001$; In the first row (nested across EV) the interaction with EV is
 1335 visible, i.e. the higher the EV, the stronger our effects of interests were.

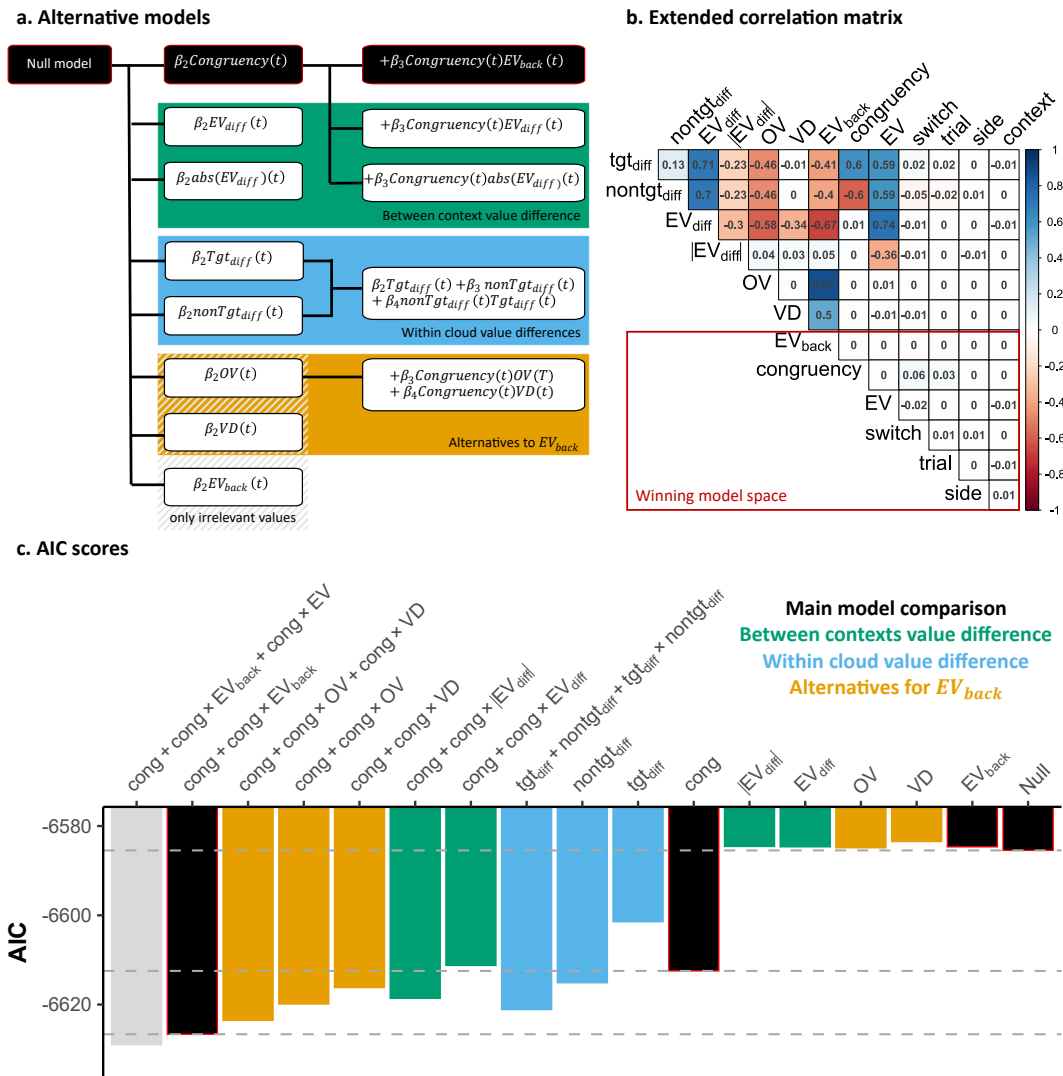


Figure S3: Alternative RT models, extended RT model comparisons and correlation matrix of all regressors, related to Fig 2.

1336 **Figure S3: Alternative RT models, extended RT model comparisons and correlation matrix of all**
 1337 **regressors, related to Fig 2.**

1338 **a.** Alternative mixed effect models, each represented as a row which lists main factors of interest. We clustered
 1339 different alternative models into three classes: *Green models* included factors that reflected the difference between
 1340 the expected values of both contexts ($EV - EV_{back}$, including unsigned EV factors); *blue* models include instead
 1341 factor that reflect the value-difference between context within each cloud where 'tgt' (target) is the chosen
 1342 cloud with the highest value according to the relevant context and *orange* models included two alternative
 1343 parameterization of values in the non-relevant context: irrelevant features' Value Difference (VD) and Overall
 1344 Value (OV), which are also orthogonal to Congruency (Cong), and to each other. *In black* is the main model
 1345 comparison as presented in the main text. **b. Extended correlation matrix.** Averaged correlation across subjects
 1346 of all scaled regressors for accurate 2D trials (models' input). Marked in red rectangle are main factors of the
 1347 experiment which are orthogonal by design and used for the model comparison reported in the Main Text. **c. AIC**
 1348 **scores.** We tested different alternatives shown in (a) in a stepwise hierarchical model comparison, as in the main
 1349 text. Each bar represents the AIC (y-axis) of a different model (x-axis) where the labels on the x-axis depict the
 1350 added terms to the Null model for that specific model. The Null model included nuisance regressors and the main

1351 effect of EV (see ν and β_1 in Eq. 2). The models described in the main text are shown in black. The gray model
1352 includes the additional term for Congruency \times EV. Dashed lines correspond to the AIC values of the models used
1353 in the main text. Importantly, no main effect representing only the contextually irrelevant values (VD, OV, EV_{back})
1354 nor the difference between the EVs (EV_{diff} , $|EV_{diff}|$, also when excluding EV from the null model, not presented)
1355 improved model fit over the Null model. This supports our finding that neither large irrelevant values, nor their
1356 similarity to the objective EV, influenced participants' behavior. Similar to EV_{back} , factors from the green and
1357 orange clusters are also orthogonal to Congruency, which allowed us to test their interaction. Factors from the
1358 blue cluster highly correlate with both Congruency (and EV_{back}) and therefore were tested separately. Non of the
1359 alternatives provided a better AIC score (y axis, lower is better).

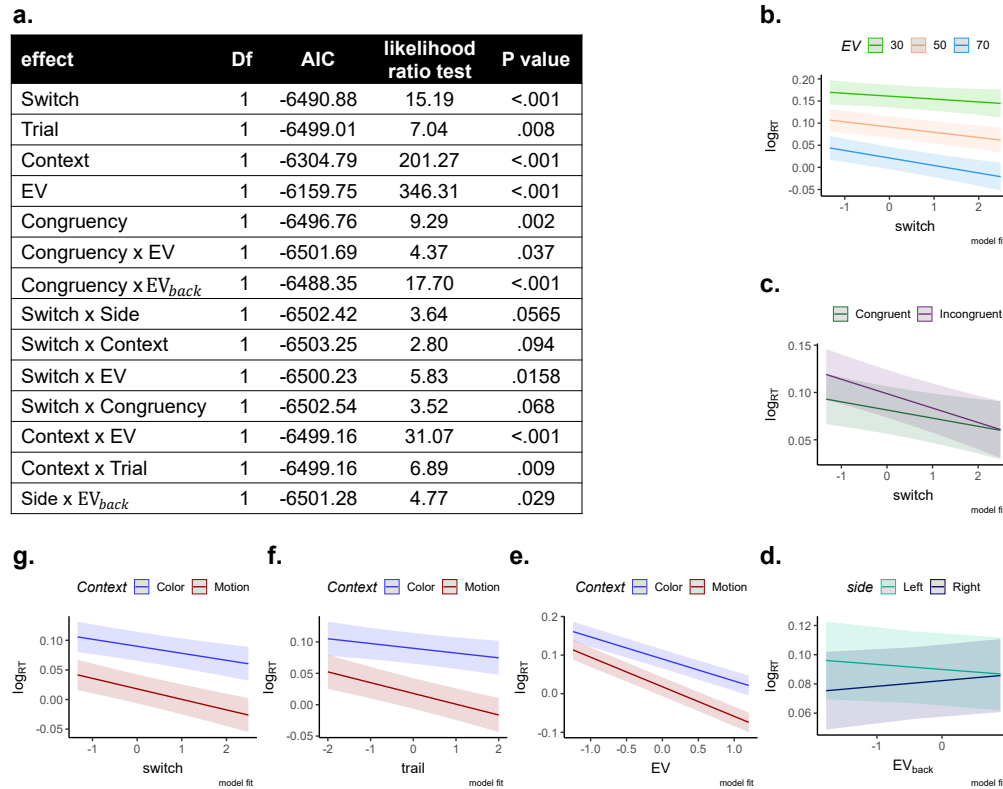


Figure S4: Exploratory analysis of RT model presented in Main Text, related to Fig 2.

1360 **Figure S4: Exploratory analysis of RT model presented in Main Text, related to Fig 2.**

1361 **a.** The table presents the individual contribution of terms taken from Eq. 2 and all possible two-way interactions
 1362 to the model fit using the drop1 function in R [57]. In short, this exploratory analysis started with a model that
 1363 included all main effects from Eq. 2 and all possible 2-way interaction between them and tested which terms
 1364 contribute to the fit. If a term did not improve fit, it was dropped from the model. Presented are all effects
 1365 with a p value less than $p < .01$. **b-g.** Model fits of all effects with $p < .1$. X-axes are normalized (as in the
 1366 model) and y-axes reflect RTs on a log scale (model input). Clockwise from the top: RTs became progressively
 1367 faster with increasing trials since the context switch. This effect was possibly stronger for higher EV (b) and for
 1368 incongruent trials (c). We note that our experiment was not designed to test the effect of the switch. (d) An
 1369 interaction of Side and EV_{back} was found, for which we offer no explanation. Panels (e) to (g) reflect interaction
 1370 of context with EV (e), trial (f), and switch (g). We note that due to the used perceptual color space there
 1371 might be a context-specific ceiling effect in RTs due to training throughout the task which could have induced
 1372 effects of context. Specifically, since dots start gray and slowly 'gain' the color, it might take a few frames until
 1373 there is any evidence for color. However, the motion could be theoretically detected already on the second frame
 1374 (since coherence was very high). This could explain why some effects that represent decrease in RT might hit a
 1375 boundary for color (and not motion). Crucially, we refer the reader to supplementary Fig S2 where the main model
 1376 comparison hold also when we ran the model nested within the levels of Context

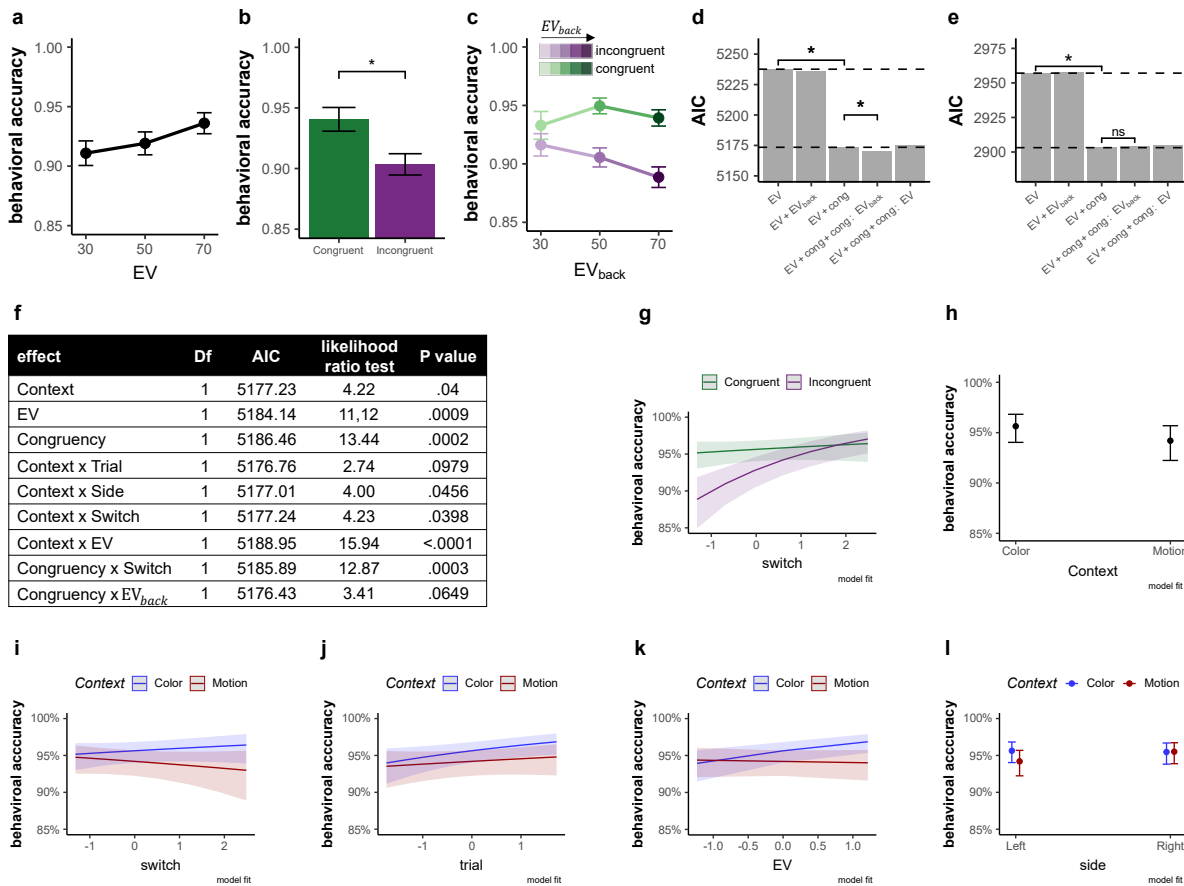


Figure S5: Behavioral accuracy results: related to Fig 2.

1377 **Figure S5: Behavioral accuracy results: related to Fig 2.**

1378 **a.** Comparison of accuracy (y-axis) for each level of EV (x-axis) showed that participants were more accurate for
 1379 higher EV, $p = .001$. **b.** Comparison of congruent versus incongruent trials also revealed a performance benefit of
 1380 the former, $p = .001$. **c.** The effect of Congruency was modulated by EV_{back} , i.e. the more participants could
 1381 expect to receive from the ignored context, the less accurate they were when the contexts disagreed (x axis, shades
 1382 of colours). Further investigations revealed that the modulation of EV_{back} is likely limited to Incongruent trials
 1383 ($\chi^2_{(1)} = 6.91$, $p = .009$, when modeling only Incongruent trials), yet does not increase accuracy for Congruent
 1384 trials ($\chi^2_{(1)} = 0.07$, $p = .794$, when modeling only congruent trials), likely due to a ceiling effect. Error bars in
 1385 panels a-c represent corrected within subject SEMs [39, 40]. **d.** Hierarchical model comparison of choice accuracy,
 1386 similar to the RT model reported in the main text. These analyses showed that including Congruency improved
 1387 model fit ($p < .001$). Including the additional interaction of Congruency \times EV_{back} improved the fit even more
 1388 ($p = .03$). **e.** We replicated the choice accuracy main effect in an independent sample of 21 participants outside of
 1389 the MRI scanner, i.e. including Congruency improved model fit ($\chi^2_{(1)} = 55.95$, $p < .001$). We did not find a main
 1390 effect of EV on accuracy in this sample ($\chi^2_{(1)} = 0.93$, $p = .333$). The interaction term Congruency \times EV_{back} did
 1391 not significantly improve fit in this sample. Modeling only Incongruent trials, as above, revealed that EV_{back} had a
 1392 marginal effect on accuracy ($\chi^2_{(1)} = 2.90$, $p = .088$). Near-ceiling accuracies in Congruent trials in combination
 1393 with a smaller sample might have masked the effects. **f.** The table presents the individual contribution of terms
 1394 taken from Eq. 3 and all possible two-way interactions to the model fit using the drop1 function in R [57]. In
 1395 short, this exploratory analysis started with a model that included all main effects from Eq. 3 and all possible
 1396 2-way interaction between them and tested which terms contribute to the fit. If a term did not improve fit, it was
 1397 dropped from the model. Subsequent panels present all the effects corresponding to $p < .01$. Note that this is a

1398 non-hypothesis driven exploration of the data and that accuracy was very high in general throughout the main
1399 task. **g.** Accuracy as a function of time since switch. Akin to RTs, accuracy increased with number of trials since
1400 the last context switch, mainly for incongruent trials. **h.** Context effect on accuracy. According to the exploratory
1401 model, participants were slightly more accurate in color than in motion trials. However, a direct paired t test
1402 between average accuracy of color compared to motion was not significant ($t_{(34)} = 0.96, p = .345$) **i-l.** Depicted
1403 are some minor interactions of no interest with Context, according to the exploratory model.

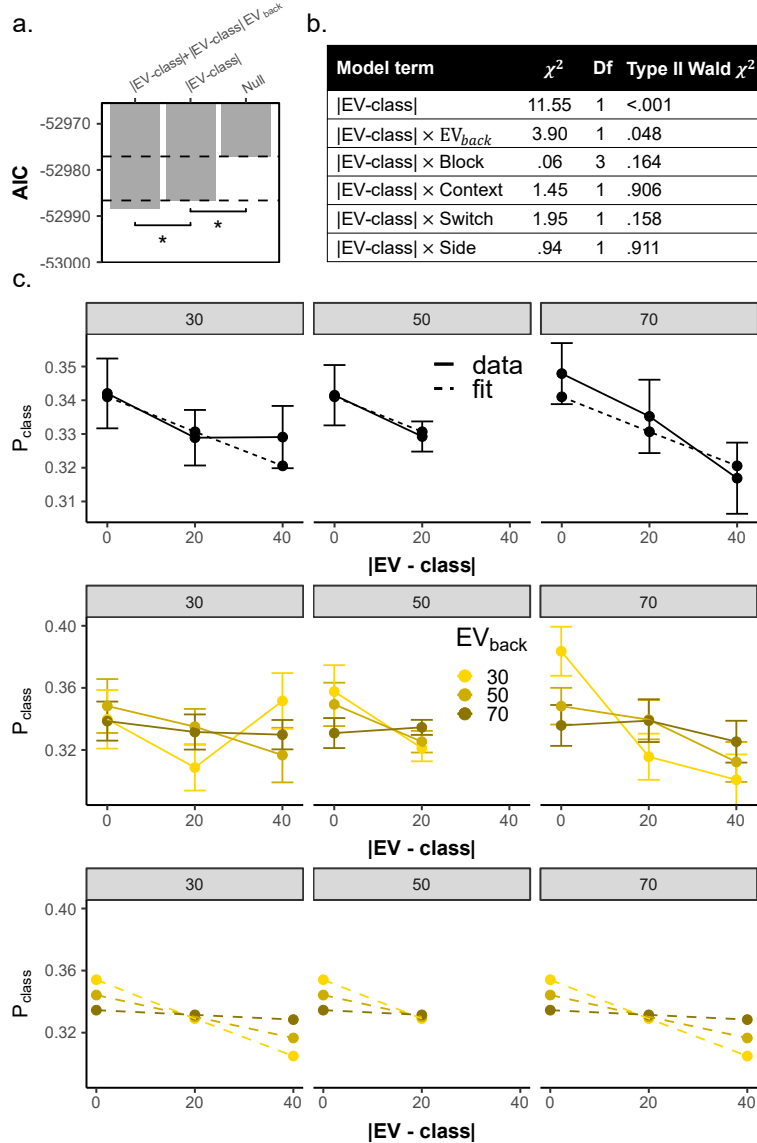


Figure S6: Supplementary information for value similarity analysis: related to Fig. 4

1404 **Fig. S6: Supplementary information for Value similarity analysis: related to Fig. 4.**

1405 **a.** Main value similarity model comparison replicated when fitting the models to unaveraged data. Adding a term
 1406 for |EV-class| improved model fit (LR test with added term: $\chi^2_{(1)} = 11.56$, $p < .001$). Adding an additional term
 1407 for |EV-class| \times EV_{back} further improved the fit ($\chi^2_{(1)} = 3.86$, $p = .049$), as in the model reported in the main
 1408 text (Fig. 4b). **b.** Effect of Nuisance regressors on unaveraged data (t, Side, Switch and Context). Same as
 1409 Congruency and EV_{back} , all of the nuisance regressors don't discriminate between the classes, but rather assign
 1410 the same value to all three probabilities from that trial (which sum to 1). We therefore tested if any of them
 1411 modulated the value similarity effect. As can be seen in the table, none of the nuisance regressors modulated the
 1412 value similarity effect. **c.** Replication of the value similarity model comparison reported in the main text, averaged
 1413 across nuisance regressors and nested within the levels of EV, i.e. including EV-specific intercepts nested within
 1414 each within each subject level ($\zeta_{0_{kv}}$, see Online Methods). As in the analysis reported in the Main Text, adding a
 1415 main effect for |EV-Class| improves model fit ($\chi^2_{(1)} = 16.15$, $p < .001$, first row) as well as adding an additional
 1416 interaction term |EV-class| \times EV_{back} ($\chi^2_{(1)} = 6.16$, $p = .013$, middle row shows data, bottom row shows model fit.
 1417 Error bars represent corrected within subject SEMs [39, 40])

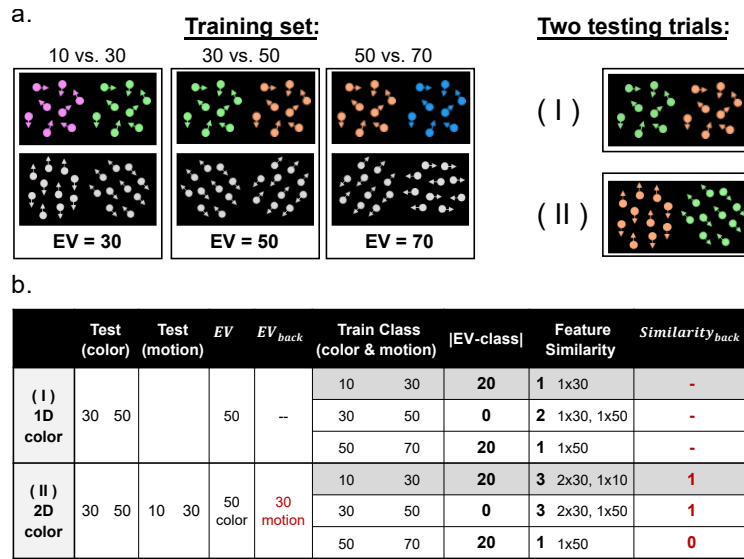
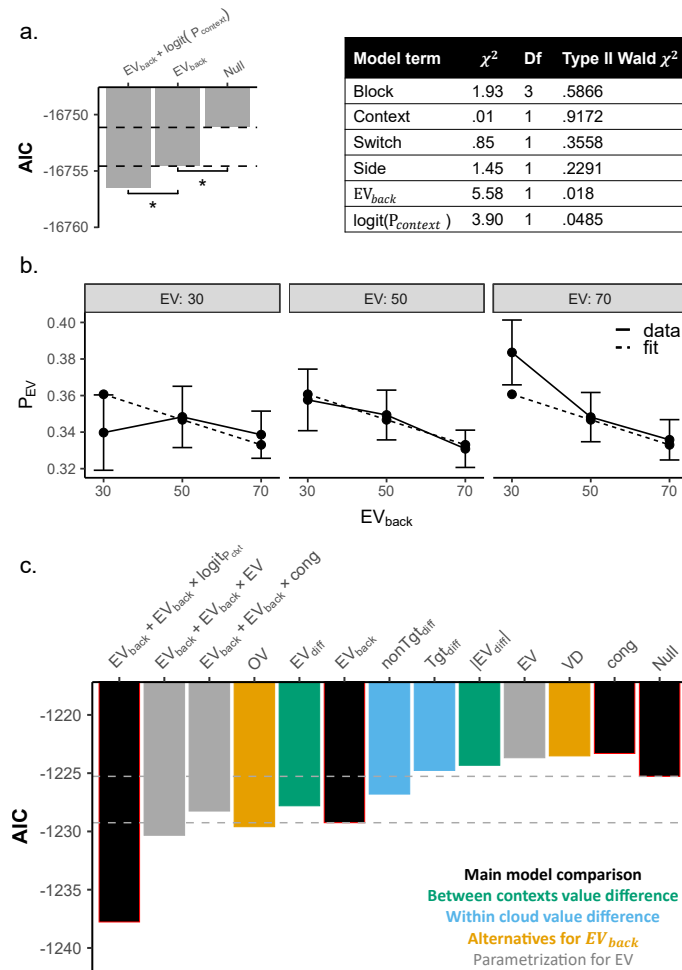


Figure S7: Supplementary information for perceptual similarity analysis: related to Fig. 4

1418 **Fig. S7: Supplementary information for perceptual similarity analysis: related to Fig. 4.**
 1419 **a.** Left: training set consisting of 1D trials provided for the classifier for each class (in the experiment the sides
 1420 were pseudorandomised). Note that each class had the same amount of color and motion 1D trials and that the
 1421 value difference between the values was always 20. Right: two examples of 2D trials that constituted the classifier
 1422 test set. **b.** The table illustrates the calculation of feature similarity between classifier test and training in two
 1423 example trials in one 1D and one 2D trial. Specifically, shown are the corresponding values and features for each
 1424 trial with the predicted values at each class for the parameters value similarity ($|EV\text{-class}|$), feature similarity
 1425 and similarity_{back}. Feature similarity encodes the perceptual overlap between the shown test example and the
 1426 training examples underlying with each value class. The first row shows a case in which the classifier was tested
 1427 on a 1D green vs. orange color trial (30 vs 50, EV = 50). Considering in this case for instance the predicted
 1428 probability that EV=30, the table illustrates the training example underlying the EV = 30 cases (10 vs 30, dark
 1429 gray shading), the $|EV\text{-class}|$ (here: 20, because 50-30), and the feature similarity i.e. how many features from the
 1430 training class appeared in the test example (here: 1). The second row shows a 2D color trial, reflecting the same
 1431 value based choice between 30 and 50. The value similarity between training and test stays the same as for the
 1432 1D trial shown above. However, the feature similarity between test and training changes because of the motion
 1433 features. If we take class 30 for example (which is 10 vs 30, dark gray shading), the feature 30 appeared twice
 1434 (color and motion) and the feature 10 appeared once (motion), i.e. feature similarity now takes on the value 3.
 1435 Similarity_{back} was used to test a perceptual-based alternative to the EV_{back} parameter. Similarity_{back} takes on 1 if
 1436 the perceptual feature corresponding to the EV_{back} appeared in the training class and 0 otherwise (red text in
 1437 table). As described in the main text, none of the perceptual-similarity encoding alternatives provided a better fit
 1438 than the reported models that focused on the values the features represent.



1439 **Fig. S8: Modelling probability assigned to the EV class: related to Fig. 5.**

1440 **a.** We replicated the main results using the unaveraged data. The Null model was: $P_{t,EV}^k = \beta_0 + \gamma_{0k} + \nu_1 side(t) +$
 1441 $\nu_2 switch(t) + \nu_3 context(t)$, where $P_{t,EV}^k$ is the probability assigned to the class corresponding to the EV of trial
 1442 t for subject k , β_0 and γ_{0k} represent global and subject-specific intercepts. Side, Switch and Context are the same
 1443 as in the RT model (Eq. 2); None of these variables had a main effect, $p > 0.4$ (see table, right). The factor *trial*
 1444 could not be included due to model convergence issues. Adding a term representing EV_{back} improved model fit (LR
 1445 test including term: $\chi_{(1)}^2 = 5.42$, $p = .019$). Adding an additional term for context decodability further improved
 1446 the fit ($\chi_{(1)}^2 = 3.9$, $p = .048$). The table (right) displays the Type 2 Wald χ^2 test for all main effects from the
 1447 model. **b.** Depicted is the effect of EV_{back} (x-axis) on the probability assigned to the EV class (P_{EV} , y axis). Solid
 1448 lines represent the data and dashed lines the model fit of a model that included random effects of subject and EV
 1449 nested within subject (data averaged across nuisance regressors, adding a main effect for EV_{back} improved model
 1450 fit ($\chi_{(1)}^2 = 5.99$, $p = .014$). Error bars represent corrected within subject SEMs [39, 40]. **c.** Similar to our analysis
 1451 of alternative models of RT, we clustered models reflecting alternative explanations into three conceptual groups
 1452 (see color legend; cf. Fig. S3a). All models were fitted to the probability assigned to the objective EV in accurate
 1453 2D trials, similar to Eq. 5. Each column represents the AIC (y-axis) of a different model (x-axis) where the labels
 1454 on the x-axis depict all the main effects included in that specific model (i.e. added to the Null, i.e. Eq. 5 without
 1455 any main effects). We found no evidence that any other parameters explain the data better than the ones we
 1456 used in the main text. Specifically, only including main effect of EV_{back} , Overall Value of the irrelevant values
 1457 (OV) and the difference of both EVs (EV_{diff}) provided a better AIC score than the Null model. Note that adding

1458 OV (-1229.6) only slightly surpassed EV_{back} (-1229.26). Crucially, the correlation of EV_{back} and OV is very high
1459 ($\rho = .87$, see main text). We then looked at possible interactions with the EV_{back} effect. Congruency did not seem
1460 to modulate the main effect of EV_{back} and adding an interaction term $EV \times EV_{\text{back}}$ provided a slightly better AIC
1461 (-1230.33), yet this effect was not significant (LR test: $\chi^2_{(1)} = 3.08$, $p = .079$). Section (b) also visualizes this
1462 effect. Lastly, adding a term for the Context decodability provided the lowest (i.e. best) AIC score.

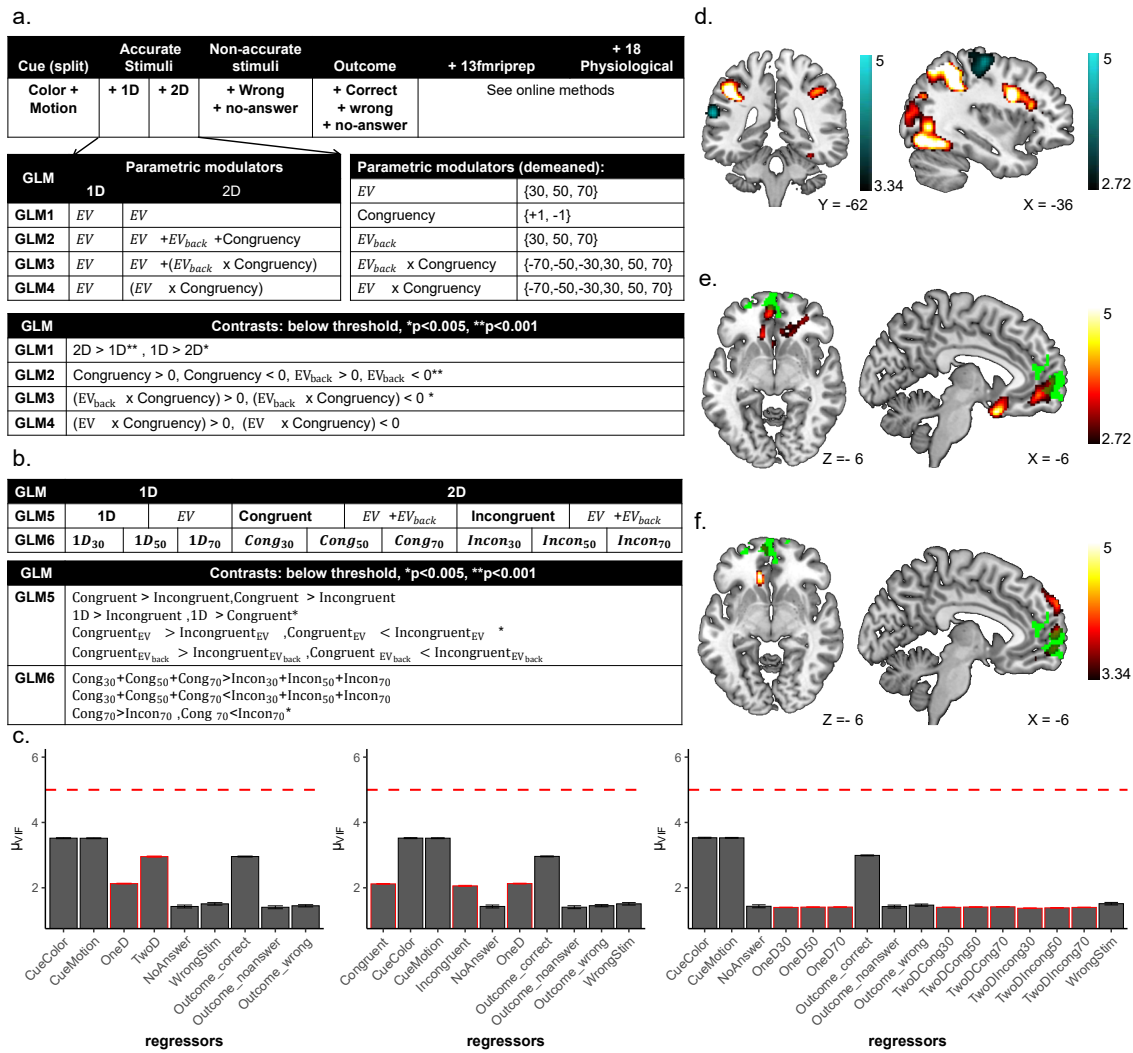


Figure S9: Additional univariate results.

1463 **Fig. S9: Additional univariate results, related to Fig. 8.**

1464 **a.** Visualization of GLMs described in the main text. The tables depict the structure of GLMs1-4 which were
 1465 mainly motivated by the behavioral analysis; onset regressors are shown in the top table, parametric modulators
 1466 assigned to 1D and 2D onsets (middle-left), the values they were modeled with (demeaned, middle-right) are shown
 1467 below. The contrasts of interest are shown in the bottom table. The GLMs differed only in their modulations
 1468 of the 2D trials: GLM1 included only modulators of the objective outcome, GLM2 included one modulator for
 1469 Congruency and one for EV_{back}, GLM3 included a modulator for the Congruency × EV_{back} interaction and GLM4
 1470 included instead of the EV modulator a modulator of the EV × Congruency interaction. In the contrast table
 1471 (bottom) contrasts that only revealed effects at a liberal threshold of $p < .005$ are marked with one star, and
 1472 contrasts significant at $p < .001$ are marked with **. **b.** We constructed additional GLMs to verify the results of
 1473 GLMs 1-4. In GLM5 we split the onset of 2D trials into congruent and incongruent trials and assigned a parametric
 1474 modulator of EV and EV_{back} to each. As in GLM2, we found no effect of congruency; no voxel survived when
 1475 contrasting the congruency onsets nor their EV_{back} modulators. Only the contrast Congruent_{EV} < Incongruent_{EV}
 1476 revealed a weak cluster in the right visual cortex (peak 38,-80,16, $p < 0.005$ not presented). In GLM6 we split the
 1477 onsets of the 1D and 2D trials by levels of EV and the 2D trials further by Congruency. No Congruency main effect
 1478 survived correction. Only when the onsets of Congruent and Incongruent 2D trials with EV=70 were contrasted, a

1479 cluster in the primary motor cortex was found (also at $p < .005$). Unsurprisingly, this cluster largely overlapped
1480 with the Congruency \times EV_{back} effect reported in the Main Text. Except the contrast of 1D > Congruent (see
1481 Main Text) none of the other contrasts shown in the table revealed any cluster, even at $p < .005$. **c.** Variance
1482 Inflation Factor (VIF) of the different regressors. None of the regressors (x axis) had a mean VIF value (y axis)
1483 across blocks and participants above the threshold of 4. Regressors involved in GLMs 1-4 shown on the left;
1484 GLM5 and GLM6 are shown in the middle and on the right, respectively. See Online Methods for details. **d.**
1485 Overlap of effects of EV_{back} and trial type (2D > 1D). Main effects of EV_{back}<0 (GLM2, $p < 0.001$ FDR cluster
1486 corrected, left, blue shades) and EV_{back} X Congruency < 0 (GLM3, $p < 0.005$, FDR cluster corrected, right, blue
1487 shades, t values) did not overlap with the 2D network (red shades in both panels, t values). **e.** Main effect of 1D
1488 > 2D. A stronger signal in vmPFC for 1D over 2D trials revealed weak activation in a PFC network ($p < .005$,
1489 red shades,t values). This included the vmPFC (our functional ROI is depicted in green). **f.** Stronger signal in
1490 vmPFC for 1D over congruent but not incongruent trials. When we split the onset of the 2D into Congruent and
1491 Incongruent trials (GLM5), we found no significant cluster for the 1D > Incongruent contrast, but an overlapping
1492 and stronger cluster for the 1D > Congruent contrast ($p < .001$, FDR cluster corrected, red shades, t values). We
1493 found very similar results when contrasting the onsets of 1D and Congruent in GLM6 (not presented), confirming
1494 the same results also when controlling for the number of trials for each level of EV (i.e. $1D_{30}+1D_{50}+1D_{70}>$
1495 $\text{Congruent}_{30}+\text{Congruent}_{50}+\text{Congruent}_{70}$). Our functional ROI is depicted in green.

Table S1: Detailed univariate results: Clusters for whole brain univariate analysis, related to Fig. 8. Presented are the closest labels to the local maxima of each cluster and each contrast using AAL3v1 [84–86]. All contrasts are FDR cluster corrected. p and k values presented for each cluster.

Anatomical region		Peak (MNI)			peak		
Label	Distance	X	Y	Z	Cluster size	t\$_{34}\$	p\$_{unc}\$
EV_{1D} > 0 ∩ EV_{2D} > 0, p<.001, k = 280							
R Inferior Temporal Gyrus	4.90	60	-18	-14	1770	6.53	< .0001
R Middle Temporal Gyrus	0	50	-6	-20		5.49	< .0001
R Middle Temporal Gyrus	0	56	-30	-8		5.27	< .0001
R Superior Frontal Gyrus, medial Orbital	0	8	68	-12	1045	6.09	< .0001
L Inferior Frontal Gyrus pars orbitalis	0	-50	30	-10		4.67	< .0001
L Superior Frontal Gyrus	0	-24	58	-6		4.35	< .0001
L Middle Temporal Gyrus	0	-60	-30	-6	1318	5.85	< .0001
L Middle Temporal Gyrus	0	-66	-24	-8		5.78	< .0001
L Hippocampus	2	-40	-26	-12		4.96	< .0001
L Angular Gyrus	0	-50	-60	38	875	5.58	< .0001
L Angular Gyrus	0	-46	-52	30		4.86	< .0001
L Angular Gyrus	0	-46	-70	34		3.66	.0002
L Middle Cingulate & Paracingulate Gyri	0	-4	-40	44	1065	5.51	< .0001
L Posterior Cingulate Gyrus	0	0	-44	32		4.52	< .0001
R Middle Cingulate & Paracingulate Gyri	0	12	-48	32		4.52	< .0001
L Hippocampus	0	-18	-6	-20	280	4.59	< .0001
L Olfactory Cortex	2	-10	6	-18		4.34	< .0001
R Angular Gyrus	0	50	-56	30	474	4.27	< .0001
R Superior Temporal Gyrus	0	62	-54	22		4.26	< .0001
2D > 1D, p<.001, k=158							
L Superior Occipital Gyrus	2.83	-28	-76	38	5367	8.71	< .0001
L Inferior Occipital Gyrus	0	-48	-76	-4		7.69	< .0001
L Superior Parietal Gyrus	0	-28	-66	52		7.62	< .0001
L Precentral Gyrus	0	-46	4	30	1766	7.69	< .0001
L Inferior Frontal Gyrus, triangular part	0	-44	34	22		5.88	< .0001
L Inferior Frontal Gyrus, triangular part	0	-40	26	22		5.59	< .0001
R Inferior Parietal Gyrus	0	32	-56	54	3876	7.23	< .0001
R Fusiform Gyrus	0	30	-76	-10		7.16	< .0001
R Inferior Temporal Gyrus	0	48	-70	-8		7.13	< .0001
R Inferior Frontal Gyrus, triangular part	0	48	26	26	616	5.17	< .0001
R Precentral Gyrus	0	48	8	32		4.50	< .0001
R Precentral Gyrus	0	38	2	30		4.23	.0001
L Supplementary Motor Area	0	-8	14	50	159	4.69	< .0001
EV_{mathrmback} < 0, p<.001, k = 240							
L SupraMarginal Gyrus	2	-62	-38	22	240	4.50	< .0001
L Superior Temporal Gyrus	0	-60	-32	10		4.26	.0001
L Superior Temporal Gyrus	0	-60	-22	8		3.71	.0004
Congruency × EV_{back} < 0, p<.005, k=632							
L Postcentral Gyrus	6.93	-36	-18	60	632	4.03	.0002
L Postcentral Gyrus	0	-48	-22	52		3.11	.0019
L Postcentral Gyrus	0	-24	-20	74		3.08	.0020
EV_{1D} + EV_{2D} > 0, within functional ROI, p<.001, k=979							
R Anterior Orbital Gyrus	4.47	8	68	-12	979	7.89	< .0001
L Superior Frontal Gyrus, Medial Orbital	2	-6	68	-12		6.86	< .0001
L Superior Frontal Gyrus, Medial	0	-10	64	2		5.86	< .0001